Two-Dimensional Halide Perovskite Lateral Epitaxial Heterostructures

Enzheng Shi[1‡], Biao Yuan[2‡], Stephen B. Shiring[1], Yao Gao[1], Akriti[1], Yunfan Guo[3], Cong Su[4], Minliang Lai[5], Peidong Yang[5,6,7], Jing Kong[3], Brett M. Savoie[1]*, Yi Yu[2]*, Letian Dou[1,8]*

[1]Davidson School of Chemical Engineering, Purdue University, West Lafayette, Indiana 47907, United States.

[2]School of Physical Science and Technology, ShanghaiTech University, Shanghai 201210, China.
[3]Department of Electrical Engineering and Computer Science, Massachusetts Institute of Technology, Cambridge, MA, 02139, United States.

[4]Research Lab of Electronics (RLE), Massachusetts Institutes of Technology, Cambridge, MA 02139, United States.

[5]Department of Chemistry, University of California, Berkeley, CA 94720, United States.

[6]Materials Sciences Division, Lawrence Berkeley National Laboratory, Berkeley, CA 94720, United States.

[7]Department of Materials Science and Engineering, University of California, Berkeley, CA 94720, United States.

[8]Birck Nanotechnology Center, Purdue University, West Lafayette, Indiana 47907, United States.

* E-mail: dou10@purdue.edu (L.D.); yuyi1@shanghaitech.edu.cn (Y.Y.); bsavoie@purdue.edu (B.M.S.)

‡These authors contributed equally to this work.

Atomically sharp epitaxial heterostructures based on oxide perovskites, III-V, II-VI, and transition metal dichalcogenides semiconductors form the foundation of modern electronics and optoelectronics[1-7]. As an emerging family of tunable semiconductor materials with exceptional optical and electronic properties, halide perovskites are attractive for applications in next-generation solution-processed solar cells, LEDs, photo/radiation detectors, lasers, *etc*[8-15]. The inherently soft crystal lattice allows for greater tolerance to lattice mismatch, making them promising for heterostructure formation and semiconductor integration[16,17]. However, epitaxial growth of atomically sharp heterostructures of halide perovskites has not yet been achieved so far owing to two critical challenges. First, the fast intrinsic ion mobility in these materials leads to interdiffusion and large junction widths[18-21]. Second, poor chemical stability in these materials leads to decomposition of prior layers during the fabrication of the subsequent layers. Facile ion diffusion and poor stability are currently limiting the commercialization of any halide perovskite-based electronic devices[22,23]. Therefore, understanding the origins of the halide perovskite instability and identifying effective approaches to suppress ion diffusion are of great significance and urgency[24-26]. Here, we report an effective strategy to substantially inhibit in-plane ion diffusion in two-dimensional (2D) halide perovskites *via* incorporation of rigid π-conjugated organic ligands. For the first time, we demonstrate highly stable and widely tunable lateral epitaxial heterostructures, multi-heterostructures, and superlattices of 2D halide perovskites *via* a solution-phase synthetic strategy. Near atomically sharp interfaces and epitaxial growth are revealed from low dose aberration-corrected high-resolution transmission electron microscopy (AC-HRTEM) characterizations. Molecular dynamics (MD) simulations reveal that the suppressed halide anion diffusivity is attributed to a combination of reduced heterostructure disorder and larger vacancy formation energies for 2D perovskites with conjugated ligands. These findings represent critical fundamental insights into the immobilization and stabilization of halide perovskite semiconductor materials and provide a new materials platform for complex and molecularly thin superlattices, devices, and integrated circuits.

Two-dimensional (2D) halide perovskites exhibit high photoluminescence quantum yield, long carrier lifetime and diffusion length, and remarkable optoelectronic tunability owing to their structural and compositional flexibility[27-34]. These 2D perovskites form quantum wells composed of periodically repeating organic and inorganic layers along the out-of-plane direction, providing further structure and property tunability[35,36]. In this work, the synthesis of 2D halide perovskite lateral heterostructures is performed *via* a solution-phase sequential growth approach, as shown in Supplementary Fig. 1. In general, halide perovskites are susceptible to damage after two or more sequential growth steps, particularly when the subsequent growth is performed in more aggressive conditions (*e.g.* a higher temperature or a more polar solvent) than the prior step. To eliminate the possibility of damaging the existing crystals, the subsequent growth is performed under a relatively

milder growth condition, *i.e.*, lowering the growth temperature or adding more antisolvent in the precursor's solution. Thus, the subsequent halide perovskites are nucleated along the edges of the prior 2D crystals, thereafter, forming concentric square/rectangular 2D lateral heterostructures directly on the SiO_2/Si substrate. By controlling the solution concentration, growth temperature and growth time, the lateral size and vertical thickness of the 2D crystal can be controlled (Supplementary Figs. 2-4).

As shown in Fig. 1a, b, two types of lateral 2D halide perovskite heterostructures are created using different organic ligands: a conjugated ligand based on bithiophenylethylammonium ($2T^+$, Fig. 1a and Supplementary Table 1) and a widely studied alkyl ligand butylammonium (BA^+, Fig. 1b). The heterostructures exhibit two concentric regions with slight optical contrast and distinct PL emissions, including the central square/rectangular bromide region and the peripheral iodide region with a uniform width of 1~2 μm for the iodide region (Fig. 1c-f). For $(2T)_2PbI_4$-$(2T)_2PbBr_4$ heterostructures, no PL emission is detected from the central $(2T)_2PbBr_4$ region, which is attributed to type-II band alignment between the inorganic $[PbBr_4]^{2-}$and organic ligand $2T^+$ layers as shown in the proposed band alignment (Fig. 1a)[37]. $(2T)_2PbI_4$ has a green PL emission (Fig. 1d, i) peaking at 515 nm because of the type-I band alignment between $[PbI_4]^{2-}$and $2T^+$ layers (Fig. 1a). The creation of the $(BA)_2PbI_4$-$(BA)_2PbBr_4$ heterostructure follows a similar synthetic procedure (Fig. 1e, f). It is known that the Br-I heterostructure is not thermally stable in 3D perovskites because of the large solid-state diffusivity of Br^- and I^-. Interdiffusion of halide anions across the heterojunction can be triggered and accelerated upon mild heating[20,21]. Here, surprisingly, we found that when the conjugated 2T ligands are used, the interdiffusion between Br^- and I^- in the $(2T)_2PbI_4$-$(2T)_2PbBr_4$ heterostructure is significantly inhibited. As shown in Fig. 1g, after heating at 100 °C for 1 h, no difference is observed in the PL image, and the PL emission shift is within 1 nm (Fig. 1i, with extended temperatures and times in Supplementary Fig. 5), suggesting negligible halide interdiffusion across the $(2T)_2PbI_4$-$(2T)_2PbBr_4$ interface. In contrast, halide interdiffusion is fast in the reference heterostructure $(BA)_2PbI_4$-$(BA)_2PbBr_4$. As shown in Fig. 1h, i, after 1 h of heating at 100 °C, the interface between the blue region associated with $(BA)_2PbBr_4$ and the green region associated with $(BA)_2PbI_4$ becomes blurry and there is a drastic change in the PL emission spectrum (extended temperatures and times are presented in Supplementary Fig. 6). The green peak which was initially located at 515 nm blueshifts to 496 nm, while the blue peak redshifts from 411 to 415 nm. Meanwhile, the peaks become significantly broader, indicating pronounced I/Br interdiffusion and alloying. It is estimated that the diffusion is slowed down by two to three orders of magnitude in the 2T heterostructures compared with the BA based heterostructures (Supplementary Fig. 7).

MD simulations were used to investigate the suppression of halide interdiffusion in the $(2T)_2PbI_4$-$(2T)_2PbBr_4$ heterostructure. MD simulations on heterostructures of $(2T)_2PbI_4$-$(2T)_2PbBr_4$ and $(BA)_2PbI_4$-$(BA)_2PbBr_4$ at both room and elevated temperatures are consistent with the experimental observations: for $(2T)_2PbI_4$-$(2T)_2PbBr_4$, no diffusion is observed at either

temperature, while halide diffusion across the interface is observed in $(BA)_2PbI_4$-$(BA)_2PbBr_4$ at elevated temperatures. As shown visually in Fig. 1j, k, the amount of disorder at the interface is strongly impacted by the choice of organic ligand. In $(2T)_2PbI_4$-$(2T)_2PbBr_4$, the interface remains pristine and well-ordered at elevated temperature. In contrast, interdiffusion and increased disorder are observed in the $(BA)_2PbI_4$-$(BA)_2PbBr_4$ heterojunction at elevated temperature. As comparative measures of the disorder, both the displacements of the lead atoms from the 2D perovskite plane and octahedral tilt angles were summarized from the simulations (Supplementary Fig. 8). The displacements for $(2T)_2PbI_4$-$(2T)_2PbBr_4$ are less than ~2 Å at both room and elevated temperatures; in contrast, $(BA)_2PbI_4$-$(BA)_2PbBr_4$ shows displacements >3Å and >4Å at room temperature and elevated temperatures, respectively. Consistent trends are observed in the tilt angle results, with broader distributions occurring in proximity to the heterojunction (Supplementary Fig. 9). The increased disorder at room temperature is also consistent with the reduced resolution observed for BA based compounds in the PL experiments (Supplementary Fig. 6). The larger and more rigid conjugated organic ligands are thus able to stabilize the interface and inorganic framework more effectively, while the smaller organic ligand leads to softer inorganic lattice that can accommodate the mismatch in halide sizes and facilitate halide interdiffusion.

Vacancy generation at high temperatures could also influence the interdiffusion process. For a vacancy-mediated diffusion process, the diffusion constant D can be expressed as[38]

$$D = D_0 exp(-\frac{E_a}{k_B T}) = \alpha a^2 \omega N_v$$

$$N_v = exp\,(-\frac{\Delta G}{k_B T}) = exp\,(\frac{\Delta S}{k_B}) exp\,(-\frac{\Delta H}{k_B T})$$

where N_v is the fraction of vacancies in solid; α is a geometric constant; a is the elementary jump distance; ω is the jump frequency; k_B is the Boltzmann constant; T is the absolute temperature; $\Delta H, \Delta S\ and\ \Delta G$ are enthalpy change, entropy change and Gibbs free energy change for the formation of a vacancy; respectively. The vacancy concentration N_v is usually treated as a constant for most oxide materials and ω is the only temperature-dependent factor. However, for halide materials, the vacancy formation energy is normally much lower and therefore both N_v and ω are Arrhenius activated. Taking this into consideration, Multistate Bennett Acceptance Ratio (MBAR) calculations on pure 2D perovskite systems were used to investigate halide and ligand vacancy formation ~~as a function of the ligand~~ (Fig. 1l). With the BA ligand the activation barrier to generate halide vacancies is much lower compared to the 2T ligand. Meanwhile, the free energy for creating a ligand vacancy by removing a ligand molecule from the surface is similar for both BA and 2T for a given halide species (Supplementary Fig. 10), indicating BA and 2T ligand vacancy concentrations are similar and may not play a dominant role. From these calculations, the number of ligand vacancies is expected to be similar upon heating the crystals, while a greater concentration of halide vacancies is to be expected in $(BA)_2PbI_4$-$(BA)_2PbBr_4$ heterojunctions,

which also promotes faster anion interdiffusion. Therefore, it is suggested that both the lower interfacial disorder and the lower halide vacancy concentration in 2T based perovskites likely contribute to the inhibition of the halide interdiffusion in the $(2T)_2PbI_4$-$(2T)_2PbBr_4$ heterojunctions. As suggested by the differences between the free energy calculations for ligand and halide vacancy generation, the differences in the interfacial stability is largely attributed to the identity of the ligands and not to the identity of the individual halides.

Energy dispersive X-ray spectroscopy (EDS) and selected area electron diffraction (SAED) were used to provide structural insights in the ultrathin $(2T)_2PbI_4$-$(2T)_2PbBr_4$ heterostructures. Because the heterostructures are directly grown on SiO_2/Si substrates, it is challenging to transfer the heterostructures to the TEM grids. To address this issue, we ~~creatively~~ used a sacrificial polymethyl methacrylate (PMMA) layer on the growth substrate prior to the growth of heterostructures. The growth substrate with PMMA layer was then soaked in chlorobenzene (see Methods) to release the 2D crystals facilitating easy transfer of 2D crystals to the TEM grid. The low-magnification TEM image and EDS elemental mappings of a $(2T)_2PbI_4$-$(2T)_2PbBr_4$ heterostructure (Fig. 2a$_1$-a$_5$) show that Pb is distributed uniformly throughout the heterostructure while I and Br are concentrated at peripheral and central regions, respectively. This is consistent with PL, X-ray diffraction (XRD), and scanning electron microscopy (SEM) characterizations (Fig. 1 and Supplementary Fig. 11). Hybrid perovskites are known to undergo rapid degradation under the electron beam irradiation. To avoid structural damage from the electron beams, the SAED patterns were obtained with a reduced electron dose-rate (*e.g.*, less than 0.1 $e^{-}Å^{-2}s^{-1}$). By comparing the experimental diffraction patterns with the kinematical selected area diffraction patterns, the zone axis for electron diffraction is determined to be [114] (see Supplementary Fig. 12 and related discussion). As shown in Supplementary Figs. 12 and 13, the slight difference in diffraction patterns between pure $(2T)_2PbI_4$ and $(2T)_2PbBr_4$ sheets is attributed to their lattice mismatch (5~6%, Supplementary Table 2 and Table 3). For the $(2T)_2PbI_4$-$(2T)_2PbBr_4$ interface, the SAED pattern (Fig. 2b) is composed of two sets of patterns with identical orientation from $(2T)_2PbI_4$ and $(2T)_2PbBr_4$, respectively, suggesting the epitaxial growth of $(2T)_2PbI_4$ from the $(2T)_2PbBr_4$ sheet.

To achieve a higher spatial resolution of the heterostructure interface ~~without damaging the sample~~ while minimizing the radiation damage, low dose AC-HRTEM was performed at an accelerating voltage of 80 kV (Fig. 2c, d, and Supplementary Fig. 14). In our early work, atomic resolution imaging was achieved on all inorganic halide perovskites taking the advantage of low dose AC-HRTEM[39]. Here, further incorporated with minimum dose strategy (Supplementary Fig. 14), the lattice information of radiation-sensitive hybrid organic-inorganic halide perovskites could be successfully revealed. The continuous lattice fringes can be imaged at the $(2T)_2PbI_4$-$(2T)_2PbBr_4$ interface (Fig. 2c$_1$) and its corresponding fast Fourier transform (~~F~~FT) information (Fig. 2c$_2$) is consistent with the SAED pattern (Fig. 2b), further confirming the epitaxial growth between $(2T)_2PbBr_4$ and $(2T)_2PbI_4$ at a nanometer scale. Moreover, a Fourier filtering technique was utilized to further resolve the interface. Due to the different lattice constants between the two

segments across the interface, the real-space lattice information is obtained by applying well-tuned masks in Fourier ~~transform~~ space. The masked green and red areas in Fig. 2c$_3$ correspond to the lattice information from $(2T)_2PbI_4$ (Supplementary Fig. 15b) and $(2T)_2PbBr_4$ (Supplementary Fig. 15c), respectively. By superimposing the two inverse ~~F~~FT images, the near atomically sharp interface can be better distinguished (Fig. 2c$_4$). The clear interface is also observed in the strain mapping in Supplementary Fig. 16. ~~The~~ Phase images also demonstrate the relatively uniform lattice of the $(2T)_2PbBr_4$ layer and periodic lattice deformation of the epitaxial $(2T)_2PbI_4$ layer (Supplementary Fig. 16h). In order to relax the accumulated interfacial strain and stabilize the heteroepitaxy, periodic interfacial misfit dislocations are expected[40]. This is evidenced by our direct observations from the Fourier filtered AC-HRTEM images (Fig. 2d and Supplementary Fig. 17). Figure 2d clearly demonstrates a misfit edge dislocation at an atomic level. In addition to the continuous lattice fringe along the $(40\bar{1})$ plane on both sides of the interface, the edge dislocations appear at around 15 nm intervals (Supplementary Fig. 17c). Furthermore, by analyzing multiple samples, it was found that the $(2T)_2PbI_4$ preferentially grew along two certain directions ([100] and [010]) (Supplementary Fig. 18). These observations suggest that the stable heteroepitaxy (Supplementary Fig. 19) between two similar perovskite structures is in-plane connected along the [100] and [010] directions with interfacial strain relaxed by misfit dislocations. The out-of-plane strain is likely relaxed through organic cations rearrangement.

In addition to forming misfit dislocations, strain can also be relaxed through ripple formation[7]. Here, we show that such ripples can be observed in the halide perovskite heterostructures. By simply mixing the precursors of $(2T)_2PbI_4$ and $(2T)_2PbBr_4$ together, one-pot synthesis of $(2T)_2PbI_4$ -$(2T)_2PbBr_4$ lateral heterostructures occurs with a slightly less sharp interface (Fig. 3). The spontaneous formation of $(2T)_2PbI_4$-$(2T)_2PbBr_4$ lateral heterostructures *via* the one-pot route is attributed to the large solubility difference between these two compounds (which leads to sequential precipitation from the solution during the solvent evaporation process) and the reduced nucleation energy of $(2T)_2PbI_4$ along the edge of $(2T)_2PbBr_4$ (see Supplementary Figs. 20, 21 and related discussions). Intriguingly, periodic ripples formed in the $(2T)_2PbI_4$ regions in these heterostructures, which is an indication of coherent interface free of dislocations. From the atomic force microscopy (AFM) image of the heterostructure, the height of the ripples was found to be around 40~50 nm and the inter-distance between adjacent ripples is ~1.6 μm, which agree perfectly with the 5~6% lattice strain. Interestingly, these ripple structures are significantly larger and less dense than those observed in WS_2-WSe_2 heterostructures (1 ~ 2 nm high, every ~30 nm)[7]. It is indeed surprising that the weak and soft halide perovskite lattice is able to preserve the coherency at the hetero-interface so well. Lateral interface engineering, including the interfacial dislocations and ripples discovered in 2D halide perovskite heterostructures, provides new insights and more opportunities to better control the interface integrity and associated electronic and optoelectronic properties.

We further demonstrate the general synthesis of a variety of lateral heterostructures (between different halides, metal cations, and organic ligands) and even superlattices of 2D halide perovskites following the solution-phase epitaxial growth strategy. Additional π-conjugated

organic ligands, including phenylethylammonium (PEA^+), quaterthiophenylethylammonium ($4Tm^+$) and 7-(thiophen-2-yl)benzothiadiazol-4-yl)-[2,2'-bithiophen]-5-yl)ethylammonium (BTm^+) were used. The chemical structures of all ligands in this study are listed in Supplementary Fig. 22a. Corresponding optical and PL images of each type of 2D sheet are shown in Supplementary Fig. 22b-~~S22~~k. The XRD patterns and PL spectra of these 2D sheets are summarized in Supplementary Fig. 23. Based on these, we synthesized $(BTm)_2PbI_4$-$(4Tm)_2PbI_4$ heterostructure between different organic ligands, $(2T)_2SnI_4$-$(2T)_2PbI_4$ and $(4Tm)_2SnI_4$-$(4Tm)_2PbI_4$ heterostructures between different metal cations, $(PEA)_2PbI_4$-$(PEA)_2PbBr_4$ heterostructure between different halides, $(PEA)_2SnI_4$-$(PEA)_2PbBr_4$ heterostructure between different halides and metals, $((2T)_2PbI_4$-$(2T)_2PbBr_4$ ×n, (n=2, 3, 4) superlattices, ~~$(2T)_2PbI_4$-$(2T)_2PbBr_4$-$(2T)_2PbI_4$-$(2T)_2PbBr_4$-$(2T)_2PbI_4$-$(2T)_2PbBr_4$ superlattices ($(2T)_2PbI_4$-$(2T)_2PbBr_4$ ×3),~~ and $(2T)_2SnI_4$-$(2T)_2PbI_4$-$(2T)_2PbBr_4$ multi-heterostructures (Fig. 4).

As shown in Fig. 4a, ~~the~~ lateral heterostructures can be created between two segments with distinct organic ligands (note, the sizes for two different organic ligands should be similar to reduce strain), $4Tm^+$ and BTm^+. $(4Tm)_2PbI_4$ region shows no PL emission due to the type-II band alignment between $4Tm^+$ ligand and $[PbI_4]^{2-}$ layers (Supplementary Figs. 22f and 23)[41]. The broad red PL emission from the peripheral region of the heterostructure originates from $(BTm)_2PbI_4$, which is attributed to the type-I band alignment between the $[PbI_4]^{2-}$ layer and the BTm^+ layer (Supplementary Figs. 22i and 23). In addition, the bandgap and optoelectronic properties of the halide perovskite materials can be effectively modulated by altering the metal atoms centering the $[MX_4]^{2-}$ octahedrons. By substituting Pb with Sn, 2D halide perovskite sheets were successfully synthesized with $2T^+$ and $4Tm^+$ ligands, including $(2T)_2SnI_4$ and $(4Tm)_2SnI_4$ (Supplementary Figs. 22h and 22i). In combination with the Pb-based perovskites, both $(2T)_2SnI_4$-$(2T)_2PbI_4$ and $(4Tm)_2SnI_4$-$(4Tm)_2PbI_4$ lateral heterostructures were created (Fig. 4b, c). Two distinct PL emission peaks from the $(2T)_2SnI_4$-$(2T)_2PbI_4$ heterostructure correspond to pure $(2T)_2SnI_4$ and $(2T)_2PbI_4$, and the gap in the PL image between the Pb and Sn perovskite segments is probably induced by exciton dissociation at the interface. Similarly, Pb and Sn perovskite segments in $(4Tm)_2PbI_4$-$(4Tm)_2SnI_4$ heterostructure exhibit a slight contrast in the optical image and distinct emission colors in the PL image (Fig. 4c). The peripheral region exhibits identical PL spectrum with the reference $(4Tm)_2SnI_4$ crystal (Supplementary Fig. 23). Another smaller conjugated ligand PEA^+ was used to construct a lateral heterostructure between Br and I components. As shown in Fig. 4d, the PL image and spectrum of the $(PEA)_2PbI_4$-$(PEA)_2PbBr_4$ heterostructure are close to those of $(BA)_2PbI_4$-$(BA)_2PbBr_4$, showing purple-blue color in the center and green in the peripheral region. In addition, we have also created $(PEA)_2SnI_4$-$(PEA)_2PbBr_4$ lateral heterostructures based on different halides and different metals at the same time, where the inorganic backbone is $[PbBr_4]^{2-}$ in the interior region and $[SnI_4]^{2-}$ in the peripheral region (Fig. 4e). Apart from the two-segment concentric heterostructures, more complex heterostructures have also been demonstrated. As shown in Fig. 4f, the $(2T)_2PbI_4$-$(2T)_2PbBr_4$ ×~~3~~n (n=2, 3, 4) superlattices

are synthesized through multiple repeated growth steps. As indicated in the schematic illustration and the PL image, ~~6~~4-8 concentric rectangles are formed, with green emission regions representing $(2T)_2PbI_4$ and quenched regions representing $(2T)_2PbBr_4$. Additionally, multi-heterostructures are realized by the 3rd growth of $(2T)_2SnI_4$ layer with red emission along $(2T)_2PbI_4$-$(2T)_2PbBr_4$ heterostructure (Fig. 4g). Additionally, the synthetic yields of the above-mentioned heterostructures are very high, as illustrated in the lower magnification optical and PL images (Supplementary Fig. 24). The thickness of the heterostructures ~~can be controlled~~ ranges from a single to a few unit cells as demonstrated by the AFM study (Supplementary Fig. 25).

These novel 2D heterostructures exhibit unique optical and electronic properties. For instance, as summarized in Fig. 5a-g[41-43], the band alignments of these heterostructures can be modulated by either varying the inorganic composition in the lateral in-plane direction or modifying the molecular structure in the out-of-plane direction. To the best of our knowledge, such multicomplex integrated systems have not been realized in other nanoscale heterostructures. We have fabricated a proof-of-concept thin film electrical diode based on the $(4Tm)_2SnI_4$-$(4Tm)_2PbI_4$ heterostructure with a type-II band alignment (Fig. 5h). Stable electrical rectifying behavior with a rectification ratio of $\sim 10^2$ was observed without hysteresis. Furthermore, we observed an enhanced exciton lifetime at the interface of $(2T)_2PbBr_4$-$(2T)_2PbI_4$ heterostructure and $(4Tm)_2SnI_4$-$(4Tm)_2PbI_4$ heterostructure from the fluorescence lifetime imaging measurements, which shed light upon the possibility of tuning the optoelectronic properties *via* lattice strain engineering at the interfaces of the heterostructures and superlattices (Supplementary Fig. 26 and Supplementary Table 4).

We have shown that the ion interdiffusion across 2D halide perovskite heterojunctions can be effectively inhibited by utilizing rigid conjugated ligands in the 2D perovskite structure. This suppression of ion migration enables stable and near atomically sharp interfaces to be obtained *via* sequential epitaxial growth. The generic synthesis of a wide range of 2D lateral halide perovskite heterostructures, superlattices, and multi-heterostructures not only presents a powerful platform for advancing the fundamental crystal chemistry of halide perovskites, but also opens up the possibility of further exploring their optoelectronic properties and their applications in diodes, lasers, transistors and photovoltaic devices. Particularly, the role of the conjugated organic ligands on the electronic properties of the heterostructures are worthy of further investigation. More importantly, these findings and methodologies may be extended to other classes of solution-processed 2D nanomaterials.

References

1. Lugli, P. & Goodnick, S. M. Nonequilibrium longitudinal-optical phonon effects in GaAs-AlGaAs quantum wells. *Phys. Rev. Lett.* **59**, 716–719 (1987).
2. Ahn, C. H., Rabe, K. M. & Triscone, J.-M. Ferroelectricity at the nanoscale: local polarization in oxide thin films and heterostructures. *Science* **303**, 488–491 (2004).

3. Bernevig, B. A., Hughes, T. L. & Zhang, S.-C. Quantum spin Hall effect and topological phase transition in HgTe quantum wells. *Science* **314**, 1757–1761 (2006).
4. Gong, Y. *et al.* Vertical and in-plane heterostructures from WS_2/MoS_2 monolayers. *Nat. Mater.* **13**, 1135-1142 (2014).
5. Zhang, Z. *et al.* Robust epitaxial growth of two-dimensional heterostructures, multiheterostructures, and superlattices. *Science* **357**, 788–792 (2017).
6. Sahoo, P. K., Memaran, S., Xin, Y., Balicas, L. & Gutiérrez, H. R. One-pot growth of two-dimensional lateral heterostructures via sequential edge-epitaxy. *Nature* **553**, 63–67 (2018).
7. Xie, S. *et al.* Coherent, atomically thin transition-metal dichalcogenide superlattices with engineered strain. *Science* **359**, 1131-1136 (2018).
8. Kojima, A., Teshima, K., Shirai, Y. & Miyasaka, T. Organometal halide perovskites as visible-light sensitizers for photovoltaic cells. *J. Am. Chem. Soc.* **131**, 6050–6051 (2009).
9. Tsai, H. *et al.* High-efficiency two-dimensional Ruddlesden–Popper perovskite solar cells. *Nature* **536**, 312–316 (2016).
10. Bai, S. *et al.* Planar perovskite solar cells with long-term stability using ionic liquid additives. *Nature* **571**, 245–250 (2019).
11. Cao, Y. *et al.* Perovskite light-emitting diodes based on spontaneously formed submicrometre-scale structures. *Nature* **562**, 249–253 (2018).
12. Yakunin, S. *et al.* Detection of X-ray photons by solution-processed lead halide perovskites. *Nat. Photonics* **9**, 444–449 (2015).
13. Wei, H. *et al.* Sensitive X-ray detectors made of methylammonium lead tribromide perovskite single crystals. *Nat. Photonics* **10**, 333–339 (2016).
14. Feng, J. *et al.* Single-crystalline layered metal-halide perovskite nanowires for ultrasensitive photodetectors. *Nat. Electron.* **1**, 404–410 (2018).
15. Sutherland, B. R. & Sargent, E. H. Perovskite photonic sources. *Nat. Photonics* **10**, 295–302 (2016).
16. Snaith, H. J. Present status and future prospects of perovskite photovoltaics. *Nat. Mater.* **17**, 372–376 (2018).
17. Berry, J. *et al.* Hybrid Organic-Inorganic Perovskites (HOIPs): Opportunities and Challenges. *Adv. Mater.* **27**, 5102–5112 (2015).
18. Akkerman, Q. A. *et al.* Tuning the Optical Properties of Cesium Lead Halide Perovskite Nanocrystals by Anion Exchange Reactions. *J. Am. Chem. Soc.* **137**, 10276–10281 (2015).
19. Hoffman, J. B., Lennart Schleper, A. & Kamat, P. V. Transformation of Sintered $CsPbBr_3$ Nanocrystals to Cubic $CsPbI_3$ and Gradient $CsPbBr_xI_{3-x}$ through Halide Exchange. *J. Am. Chem. Soc.* **138**, 8603–8611 (2016).
20. Lai, M. *et al.* Intrinsic anion diffusivity in lead halide perovskites is facilitated by a soft lattice. *Proc. Natl. Acad. Sci. U. S. A.* **115**, 11929–11934 (2018).
21. Pan, D. *et al.* Visualization and Studies of Ion-Diffusion Kinetics in Cesium Lead Bromide Perovskite Nanowires. *Nano Lett.* **18**, 1807–1813 (2018).
22. Park, N.-G., Grätzel, M., Miyasaka, T., Zhu, K. & Emery, K. Towards stable and commercially available perovskite solar cells. *Nat. Energy* **1**, 16152 (2016).

23. Rong, Y. *et al.* Challenges for commercializing perovskite solar cells. *Science* **361**, eaat8235 (2018).
24. Park, B. & Seok, S. I. Intrinsic Instability of Inorganic–Organic Hybrid Halide Perovskite Materials. *Adv. Mater.* **31**, 1805337 (2019).
25. Wang, Z. *et al.* Efficient ambient-air-stable solar cells with 2D–3D heterostructured butylammonium-caesium-formamidinium lead halide perovskites. *Nat. Energy* **2**, 17135 (2017).
26. Huang, Z. *et al.* Suppressed Ion Migration in Reduced-Dimensional Perovskites Improves Operating Stability. *ACS Energy Lett.* **4**, 1521–1527 (2019).
27. Dou, L. *et al.* Atomically thin two-dimensional organic-inorganic hybrid perovskites. *Science* **349**, 1518–1521 (2015).
28. Jemli, K. *et al.* Two-Dimensional Perovskite Activation with an Organic Luminophore. *ACS Appl. Mater. Interfaces* **7**, 21763–21769 (2015).
29. Connor, B. A., Leppert, L., Smith, M. D., Neaton, J. B. & Karunadasa, H. I. Layered halide double perovskites: dimensional reduction of $Cs_2AgBiBr_6$. *J. Am. Chem. Soc.* **140**, 5235–5240 (2018).
30. Leng, K. *et al.* Molecularly thin two-dimensional hybrid perovskites with tunable optoelectronic properties due to reversible surface relaxation. *Nat. Mater.* **17**, 908–914 (2018).
31. Zhang, Q., Chu, L., Zhou, F., Ji, W. & Eda, G. Excitonic properties of chemically synthesized 2D organic–inorganic hybrid perovskite nanosheets. *Adv. Mater.* **30**, 1704055 (2018).
32. Spanopoulos, I. *et al.* Uniaxial Expansion of the 2D Ruddlesden-Popper Perovskite Family for Improved Environmental Stability. *J. Am. Chem. Soc.* **141**, 5518–5534 (2019).
33. Cortecchia, D. *et al.* Broadband Emission in Two-Dimensional Hybrid Perovskites: The Role of Structural Deformation. *J. Am. Chem. Soc.* **139**, 39–42 (2017).
34. Yang, S. et al. Ultrathin Two-Dimensional Organic–Inorganic Hybrid Perovskite Nanosheets with Bright, Tunable Photoluminescence and High Stability, *Angew. Chem. Int. Ed.*, **56,** 4252 –4255 (2017).
35. Saparov, B. & Mitzi, D. B. Organic–inorganic perovskites: structural versatility for functional materials design. *Chem. Rev.* **116**, 4558–4596 (2016).
36. Ortiz-Cervantes, C. *et al.*~~, Román-Román, P. I., Vazquez-Chavez, J., Hernández-Rodríguez, M. & Solis-Ibarra, D.~~ Thousand-fold Conductivity Increase in 2D Perovskites by Polydiacetylene Incorporation and Doping. *Angew. Chem. Int. Ed.* **57**, 13882–13886 (2018).
37. Liu, C. *et al.* Tunable Semiconductors: Control over Carrier States and Excitations in Layered Hybrid Organic-Inorganic Perovskites. *Phys. Rev. Lett.* **121**, 146401 (2018).
38. Borg, R. J. & Dienes, G. J. An introduction to solid state diffusion. (Elsevier, 1988). doi:10.1016/c2009-0-22176-3.
39. Yu, Y. *et al.* Atomic Resolution Imaging of Halide Perovskites. *Nano Lett.*, **16**, 7530, (2016).
40. Matthews, J. Defects in epitaxial multilayers I. Misfit dislocations. *Journal of Crystal Growth* **27**, 118–125 (1974).

41. Gao, Y. *et al.* Molecular engineering of organic–inorganic hybrid perovskites quantum wells. *Nat. Chem.* **11**, 1151-1157 (2019).
42. Gao, Y. *et al.* Highly Stable Lead-Free Perovskite Field-Effect Transistors Incorporating Linear π-Conjugated Organic Ligands. *J. Am. Chem. Soc.* **141**, 15577-15585 (2019).
43. Silver, S., Yin, J., Li, H., Brédas, J. L. & Kahn, A. Characterization of the valence and conduction band levels of n= 1 2D perovskites: a combined experimental and theoretical investigation. *Adv. Energy Mater.* **8**, 1703468 (2018).

Supplementary information is available in the online version of the paper.

Acknowledgements: We thank L. Huang, B. Boudouris, and S. Li for helpful discussions. **Funding:** This work is supported by Office of Naval Research (Grant No. N00014-19-1-2296, Program Manager: Dr. Paul Armistead and Dr. Joe Parker), National Science Foundation (Grant No. 1939986-ECCS, Program Manager: Dr. Paul Lane) and Davidson School of Chemical Engineering, College of Engineering, and Birck Nanotechnology Center of Purdue University. TEM work is supported by the funding from NSFC (Grant No. 21805184), NSF Shanghai (Grant No. 18ZR1425200) and the Center for High-resolution Electron Microscopy (CħEM) at ShanghaiTech University (Grant No. EM02161943). J. K acknowledges the support from AFOSR FATE MURI, Grant No. FA9550-15-1-0514.
Author contributions: E.S. synthesized and characterized the 2D perovskite materials; B.Y. and Y.Y. performed TEM characterization and data analysis; S.B.S. and B.S. performed MD simulation and data analysis; Y.Gao performed organic ligand synthesis; Akriti, Y.Guo, C.S., M.L., P.Y. and J.K. participated in materials characterization and data analysis; E.S. and L.D. wrote the manuscript; all authors read and revised the manuscript.
Competing interests: Authors declare no competing interests.
Data and materials availability: All data are available in the manuscript or supplementary information. All materials are available upon request to L.D.

Methods

Solution-phase synthesis of pure 2D halide perovskite sheets

In this study, ten types of pure 2D halide perovskite sheets were synthesized *via* a quaternary solvent method.

Chemicals and reagents: Organic solvents, including anhydrous chlorobenzene (CB), dimethylformide (DMF), acetonitrile (AN) and dichlorobenzene (DCB), and solid chemicals, including lead bromide ($PbBr_2$), lead iodide (PbI_2) and tin iodide (SnI_2), were directly purchased from Sigma Aldrich. *n*-butylammonium bromide (BA·HBr), *n*-butylammonium iodide (BA·HI), phenethylammonium bromide (PEA·HBr) and phenethylammonium iodide (PEA·HI) were purchased from Greatcell Solar Ltd. All above chemicals were used as received. Other ammonium salt ligands, including 2T·HI, 2T·HBr, 4Tm·HI and BTm·HI were synthesized in our lab[41].

Synthesis of 2D halide perovskite sheets: 10 μmol of MX_2 (M=Pb or Sn; X=Br or I) and 20 μmol of L·HX (L= BA, PEA, 2T, 4Tm or BTm; X=Br or I) were dissolved in 2 mL of DMF/CB co-solvent (1:1 volume ratio) to prepare 5 mM of stock solution. The stock solution was then diluted 120 times by CB/AN/DCB co-solvent (2.5: 1: 0.01 volume ratio). 5-10 μL of diluted solution was added onto the growth substrate SiO_2 (300 nm)/Si, which was placed at the bottom of a 4 mL glass vial. Then the 4 mL vial was transferred into a secondary glass vial (20 mL) containing 3 mL of CB. After that, the secondary vial was capped and moved onto 70 ºC hot plate. The antisolvent (CB) inside the secondary vial will slow down the solvent evaporation from the substrate and facilitate the formation of large 2D halide perovskite sheets. The growth typically takes 10-30 min. Solution preparation and sheets growth were carried out in N_2-filled glovebox. The growth substrate was cleaned in piranha acid for 2 h prior to use.

The growth steps for all the halide perovskite sheets in Supplementary Fig. 22 are the same. However, the growth parameters for some sheets are slightly different. Above recipe applies to the growth of $(2T)_2PbBr_4$, $(BA)_2PbBr_4$, $(BA)_2PbI_4$ and $(PEA)_2PbBr_4$. For $(2T)_2PbI_4$, $(2T)_2SnI_4$ and $(PEA)_2PbI_4$, the stock solution was diluted 120 times by CB/AN/DCB co-solvent (9.5: 1: 0.01 volume ratio). For $(4Tm)_2PbI_4$ and $(4Tm)_2SnI_4$, the stock solution is diluted 240 times by CB/AN/DCB co-solvent (3.9: 1: 0.01 volume ratio) and the growth temperature was 90 ºC. For $(BTm)_2PbI_4$, the stock solution was diluted 1440 times by CB/AN/DCB co-solvent (7.4: 1: 0.01 volume ratio) and the growth temperature was 90 ºC.

For the quaternary solvent method for crystal growth, CB helps reduce the solubility of 2D perovskite in DMF and promotes the sheet crystallization. AN has a lower boiling point compared to CB, and 2D perovskite has a limited solubility in AN. In this case, AN evaporates more quickly and initiates the 2D perovskite nucleation at a relatively low concentration, thus decreasing the thickness of sheets. Moreover, compared to CB, DCB has a higher boiling point. The addition of DCB will avoid the gradually increasing concentration of perovskite solution with the evaporation of AN and CB, thus ensuring the uniform distribution of sheets throughout the growth substrate.

Epitaxial synthesis of 2D lateral halide perovskite heterostructures

The epitaxial growth of 2D lateral halide perovskite heterostructures was based on the above quaternary solvent method. The growth of 1st sheet is identical to above method. To eliminate the possibility of crystal damage, the subsequent growth was performed under milder growth conditions in our study, *i.e.* by lowering the growth temperature or adding more antisolvent in the solution.

$(2T)_2PbI_4$-$(2T)_2PbBr_4$ heterostructures and superlattices: The sequence of the two steps for heterostructure formation (bromide followed by iodide *vs.* iodide followed by bromide) is dictated by the solubility difference of the two halide perovskites in the solvent system. Since $(2T)_2PbBr_4$ has a lower solubility in the quaternary solvent, it is synthesized prior to $(2T)_2PbI_4$. The $(2T)_2PbI_4$ stock solution was diluted 480 times by CB/AN/DCB co-solvent (6: 1: 0.01 volume ratio) for the growth of heterostructures. After the growth of $(2T)_2PbBr_4$ sheets, the hot plate was cooled down to 50 ºC. Then 10 μL of the diluted $(2T)_2PbI_4$ solution is added on the growth substrate. The epitaxial growth of $(2T)_2PbI_4$ along $(2T)_2PbBr_4$ sheets typically takes about 30 min. The $(2T)_2PbI_4$-$(2T)_2PbBr_4$ ×n superlattices were realized by n repeated growth of $(2T)_2PbI_4$-$(2T)_2PbBr_4$

heterostructures. $(BA)_2PbI_4$-$(BA)_2PbBr_4$ heterostructures: The $(BA)_2PbI_4$ stock solution was diluted 240 times by CB/AN/DCB co-solvent (6: 1: 0.01 volume ratio) for the growth of heterostructures. After the growth of $(BA)_2PbBr_4$ sheets, the hot plate was cooled down to 50 ºC. Then 10 μL of the diluted $(BA)_2PbI_4$ solution was added on the growth substrate. The epitaxial growth of $(BA)_2PbI_4$ along $(BA)_2PbBr_4$ sheets typically takes about 30 min. $(BTm)_2PbI_4$-$(4Tm)_2PbI_4$ heterostructures: The $(BTm)_2PbI_4$ stock solution was diluted 1440 times by CB/AN/DCB co-solvent (3.2: 1: 0.01 volume ratio) for the growth of heterostructures. After the growth of $(4Tm)_2PbI_4$ sheets, the hot plate was cooled down to 50 ºC. Then 10 μL of the diluted $(BTm)_2PbI_4$ solution was added on the growth substrate. The epitaxial growth of $(BTm)_2PbI_4$ along $(4Tm)_2PbI_4$ sheets typically takes about 30 min. $(2T)_2SnI_4$-$(2T)_2PbI_4$ heterostructures: The $(2T)_2SnI_4$ stock solution was diluted 120 times by CB/AN/DCB co-solvent (9.5: 1: 0.01 volume ratio) for the growth of heterostructures. After the growth of $(2T)_2PbI_4$ sheets, the hot plate was cooled down to 50 ºC. Then 10 μL of the diluted $(2T)_2SnI_4$ solution was added on the growth substrate. The epitaxial growth of $(2T)_2SnI_4$ along $(2T)_2PbI_4$ sheets typically takes about 30 min. $(4Tm)_2SnI_4$-$(4Tm)_2PbI_4$ heterostructures: The $(4Tm)_2SnI_4$ stock solution was diluted 240 times by CB/AN/DCB co-solvent (1.8: 1: 0.01 volume ratio) for the growth of heterostructures. After the growth of $(4Tm)_2PbI_4$ sheets, the hot plate was cooled down to 80 ºC. Then 10 μL of the diluted $(4Tm)_2SnI_4$ solution was added on the growth substrate. The epitaxial growth of $(4Tm)_2SnI_4$ along $(4Tm)_2PbI_4$ sheets typically takes about 10 min. $(PEA)_2PbI_4$-$(PEA)_2PbBr_4$ heterostructures: The $(PEA)_2PbI_4$ stock solution was diluted 240 times by CB/AN/DCB co-solvent (9.5: 1: 0.01 volume ratio) for the growth of heterostructures. After the growth of $(PEA)_2PbBr_4$ sheets, the hot plate was cooled down to 50 ºC. Then 10 μL of the diluted $(PEA)_2PbI_4$ solution was added on the growth substrate. The epitaxial growth of $(PEA)_2PbI_4$ along $(PEA)_2PbBr_4$ sheets typically takes about 30 min. $(PEA)_2SnI_4$-$(PEA)_2PbBr_4$ heterostructures: The $(PEA)_2SnI_4$ stock solution was diluted 580 times by CB/AN/DCB co-solvent (35: 2: 0.01 volume ratio) for the growth of heterostructures. After the growth of $(PEA)_2PbBr_4$ sheets, the hot plate was cooled down to 50 ºC. Then 10 μL of the diluted $(PEA)_2SnI_4$ solution was added on the growth substrate. The epitaxial growth of $(PEA)_2PbI_4$ along $(PEA)_2PbBr_4$ sheets typically takes about 30 min. $(2T)_2SnI_4$-$(2T)_2PbI_4$-$(2T)_2PbBr_4$ multi-heterostructures: $(2T)_2SnI_4$ stock solution was diluted 480 times by CB/AN/DCB co-solvent (9.5: 1: 0.01 volume ratio) for the growth of multi-heterostructures. Following the growth of $(2T)_2PbI_4$-$(2T)_2PbBr_4$ heterostructures, 10 μL of the diluted $(2T)_2SnI_4$ solution was added on the growth substrate. The epitaxial growth of $(2T)_2SnI_4$ along $(2T)_2PbI_4$ sheets typically takes about 30 min.

One-pot synthesis of $(2T)_2PbI_4$-$(2T)_2PbBr_4$ heterostructures: The $(2T)_2PbI_4$ and $(2T)_2PbBr_4$ stock solutions were mixed with 1:1 ratio and diluted 480 times by CB/AN/DCB co-solvent (6: 1: 0.01 volume ratio) for the one-pot growth of heterostructures. 10 μL of the diluted solution was added on the growth substrate at a temperature of 70 ºC. Bromide and iodide components phase separated spontaneously during the evaporation of the solvents. The coherent epitaxial growth of $(2T)_2PbI_4$ along $(2T)_2PbBr_4$ sheets typically takes about 10 min.

$(4Tm)_2SnI_4$-$(4Tm)_2PbI_4$ thin film lateral heterostructure devices: $(4Tm)_2PbI_4$ (0.1 mol/L) was spin-coated on insulating substrates (quartz or SiO_2/Si), followed by 180 ºC annealing on hot plate for 5 min. Then, half of the $(4Tm)_2PbI_4$ film was removed by razor blade, and the rest of the film was

covered by a Kapton® tape. The sample was then treated by UV ozone for 30-60 min to make the exposed area hydrophilic. The Kapton® tape was removed and $(4Tm)_2SnI_4$ (0.1 mol/L) was spin-coated on the the UV ozone-treated sample, followed by 175 ºC annealing for 5 min. Finally, silver wire (diameter-120 μm) was placed at the interface region, serving as the shadow mask for Au evaporation. 50 nm Au was evaporated as the electrodes.

Characterizations

Optical imaging: The bright-field optical images were collected by a custom Olympus BX53 microscope.

PL imaging and spectra collection: Samples were excited with a light source (012-63000; X-CITE 120 REPL LAMP). The filter cube contains a bandpass filter (330-385 nm) for excitation, and a dichroic mirror (cutoff wavelength: 400 nm) for light splitting and a filter (Long pass 420 nm) for emission. The PL spectra were collected by SpectraPro HRS-300 spectrometer.

Interdiffusion calculation: We utilize a simplified one-dimensional diffusion model of Fick's second law to describe the transient concentration profile across the lateral heterostructures. The model is mathematically expressed as $\frac{\partial C}{\partial t} = \frac{\partial}{\partial x}\left(D(c)\frac{\partial C}{\partial x}\right)$. Here, C is concentration of bromide, t is heating time, x is length and D is the inter-diffusion coefficient of halides. Diffusion coefficient is calculated by using the classical Boltzmann-Matano method. The evolution of concentration profile for BA and 2T lateral heterostructures are fitted by a normal cumulative distribution function, $y = y_0 + A\int_{-\infty}^{x} \frac{1}{\sqrt{2\pi}w} e^{-\frac{(t-x_c)^2}{2w^2}} dt$. The fitted curves along with the experimental bromide concentration obtained from PL emission peaks are shown in Supplementary Fig. 7. It is to be noted that the concentration profile obtained using the edge widths and PL emissions can only be used for a rough estimation of the diffusion coefficients since no gradient is assumed across the overlaid edge widths of the lateral heterostructures. It is estimated that the diffusion coefficient of $(BA)_2PbI_4$-$(BA)_2PbBr_4$ and $(2T)_2PbI_4$-$(2T)_2PbBr_4$ lateral heterostructures are in the order of ~ 10^{-13} –10^{-12} cm^2/s and ~ 10^{-16} – 10^{-15} cm^2/s, respectively.

SEM imaging: The back-scattering SEM images were collected by a FEI TeneoVS scanning electron microscope. The acceleration voltage was 1 kV, and the acceleration current was 0.1 nA.

Powder XRD measurements: Powder XRD was measured using Panalytical Empyrean powder X-ray diffractometer with a Cu Kα source.

Atomic force microscopy (AFM): AFM images were recorded in tapping mode using a Bruker MultiMode 8 atomic force microscope.

Fluorescent lifetime imaging microscopy (FLIM) measurements: The samples with PMMA (950 PMMA A4, MICROCHEM) coating were measured with a 50× 0.55 N.A. air objective in an LSM 510 NLO AxioVert200M Confocal Laser Scanning Microscope equipped with a Mai-Tai HP tunable laser. The excitation wavelength is 405 nm, which is from the second harmonic of 810 nm (<100 fs, 80 MHZ). Lifetime measurements were performed using Becker-Hickl SPC-150 Time-Correlated Single Photon Counting. The lifetime decay was collected and analyzed using Becker-Hickl SPCM software.

Single-crystal XRD measurement: Single crystals of $(2T)_2PbBr_4$ were analyzed by a Bruker Quest diffractometer with kappa geometry, an I-μ-S microsource X-ray tube, laterally graded multilayer (Goebel) mirror single crystal for monochromatization, a Photon2 CMOS area detector and an Oxford Cryosystems low temperature device. Examination and data collection were performed with Cu Kα radiation (λ = 1.54178 Å) at 150 K.

Electric measurement: Current-voltage (I-V) characteristics were acquired by sweeping bias voltages from -10 V to 10 V and then from 10 V to -10 V based on a PS100 Lakeshore probe station with a Keithley 2400 source meter.

TEM characterizations

TEM sample preparation of pure $(2T)_2PbI_4$, $(2T)_2PbBr_4$ sheets, and $(2T)_2PbI_4$-$(2T)_2PbBr_4$ heterostructure: To transfer Pure $(2T)_2PbI_4$, $(2T)_2PbBr_4$ sheets, or $(2T)_2PbI_4$-$(2T)_2PbBr_4$ heterostructures to TEM girds, a layer of PMMA was spin-coated on the growth SiO_2/Si substrates prior to perovskite growth. The spin-coating speed was 3000 rpm and duration time was 1 min. Then Si substrates were placed on 70 ºC hot plate for 10 min to condense the PMMA and remove the residue solvent. After that, the perovskites were grown on the PMMA-coated Si.

The transfer process of perovskites from the growth PMMA/Si substrates was performed in the glove box. First, the growth substrates were dipped into CB to dissolve the sacrificial layer PMMA, which facilitates the detachment of samples from the growth substrates. Then, vortex mixing or ultrasonication was used to further detach the samples from Si substrates. Afterwards, the suspension was dropped onto the TEM grids. TEM grids were rinsed with clean CB a few times to remove the residue PMMA. Note: The TEM grids (Lacey/ carbon grids on 200 mesh copper, Ted Pella) are covered by one layer of carbon nanotube film and mono-layer graphene hybrids to mitigate electron beam damage.

TEM imaging and spectrum acquisition: The diffraction patterns were obtained on a 200 kV JEOL JEM-2100plus with a TIVPS CCD camera (TEMCam-XF416). The AC-HRTEM and EDS mapping was taken on an 80 kV aberration-corrected JEOL GrandARM equipped with a fast camera (OneView IS, Gatan). The EDS map is an intensity map based on the counts, which is proportional to the content of the element. Low accelerating voltage was utilized to enhance the contrast at low magnifications when searching for samples and locating the interface positions. The low dose-rate imaging was achieved by increasing electron beam spot size (decreasing the beam current) and reducing brightness of the electron beam (spreading the beam illumination). To avoid unnecessary electron beam damage, Minimum Dose System (MDS) was used to reduce the damage during searching for the samples and focusing.

Owing to the mechanical vibration of specimen holder and the effect of electron irradiation, there are generally minor displacements between continuously captured images, which will lower the spatial resolution of HETEM image if we simply superpose them. To correct these drifts, we use a digital micrograph script developed by D.R.G. Mitchell (http://www.dmscripting.com/stack_alignment.html). The core of the script is to measure the drift by cross correlation, thus applying measured drift to each image. Each drift measurement will produce a cross correlation value, which is a guide to whether it is working well ("1" is good, "0.5" is OK). In our case, the cross correlation values are 0.644, 0.645 and 0.647 when processing the 4

raw images. After accurate drift alignment, the images can be superposed to acquire a HRTEM image with improved signal-to-noise ratio.

TEM simulation and structural model: The kinematical SAED patterns were simulated with MacTempasX[44]. The structural models were constructed with VESTA[45].

Molecular Dynamics Simulations

For the molecular dynamics simulation of the heterojunction between Pb-Br and Pb-I organic-inorganic perovskites, the MYP model for hybrid perovskites was used[46-48] The MYP model was originally developed for Pb-I perovskites and was extended to Pb-Br perovskites, and it treats the organic-organic interactions by the standard AMBER force field, the inorganic-inorganic interactions between Pb, I, and Br by Buckingham potentials, and the organic-inorganic interactions as the sum of Buckingham, electrostatic, and Lennard-Jones 12-6 terms. As developed and reported, the charges on the metal, halide, and cation are non-integer. For our simulations, we employed integer values for these charges; the MYP non-bonded parameters were appropriately rescaled to reproduce the cohesive energy density of the unscaled simulation.

The surface cation geometries were optimized using ORCA[49] at the ωB97X-D[50]/def2-TVZP[51,52] Density Functional Theory level. The standard GAFF parameterization was used for the organic cations[53], with the cation point charges being fit against the electrostatic DFT potential (ωB97X-D/def2-TVZP) of the isolated cation with a +1 charge. LAMMPS was used for the molecular simulations[54]. All simulations used a 1 fs integration timestep and periodic boundary conditions. The particle-particle-particle-mesh (PPPM) algorithm was used for the long-range electrostatics, and LJ interactions were truncated at 15 Å. Following the MYP model, the 1-4 pairwise LJ interactions were scaled by 0.5, and the 1-4 electrostatics interactions were scaled by 0.8333.

The initial perovskite heterojunction geometry was generated by constructing an ideal perovskite monolayer composed of two domains: a 6 × 0 × 12 Pb-I domain and a 6 × 0 × 12 Pb-Br domain, for a total system sized of 12× 0 × 12 of A_2BX_4 unit cells. Halide vacancies were introduced by randomly removing 2 halide atoms. The simulation was first relaxed under the NVE ensemble for 50 ps with restrained atomic displacements of 0.01 Å per timestep. The system was then simulated for 20 ns with the Nose-Hoover thermostat and barostat, with the barostat applied only the x and z directions in order to allow the surface cations to displace from the perovskite layer, at both 298 K and 800 K. To calculate the free energy required to remove a surface cation and halide, a 6 × 0 × 6 unit cell simulation on pristine (i.e. no vacancies) Pb-Br and Pb-I perovskites was run, with a surface cation and halide displaced from their initial positions out to vacuum in 0.5 Å intervals. The system was equilibrated for 0.5 ns and then simulated for 10 ns under the NVT ensemble at 298 K for each displacement. The pymbar package, developed by the Chodera group, was used to calculate the free energies[55].

44. O'Keefe, M. A. & Kilaas, R. Advances in high-resolution image simulation. (1988).
45. Momma, K. & Izumi, F. VESTA 3 for three-dimensional visualization of crystal, volumetric and morphology data. *Journal of Applied Crystallography* **44**, 1272–1276 (2011).

46. Mattoni, A., Filippetti, A., Saba, M. I. & Delugas, P. Methylammonium Rotational Dynamics in Lead Halide Perovskite by Classical Molecular Dynamics: The Role of Temperature. *J. Phys. Chem. C* **119**, 17421–17428 (2015).
47. Mattoni, A., Filippetti, A. & Caddeo, C. Modeling hybrid perovskites by molecular dynamics. *J. Phys. Condens. Matter* **29**, 043001 (2017).
48. Hata, T., Giorgi, G., Yamashita, K., Caddeo, C. & Mattoni, A. Development of a Classical Interatomic Potential for $MAPbBr_3$. *J. Phys. Chem. C* **121**, 3724–3733 (2017).
49. Neese, F. The ORCA program system. *Wiley Interdiscip. Rev. Comput. Mol. Sci.* **2**, 73–78 (2012).
50. Chai, J.-D. & Head-Gordon, M. Long-range corrected hybrid density functionals with damped atom–atom dispersion corrections. *Phys. Chem. Chem. Phys.* **10**, 6615 (2008).
51. Schäfer, A., Horn, H. & Ahlrichs, R. Fully optimized contracted Gaussian basis sets for atoms Li to Kr. *J. Chem. Phys.* **97**, 2571–2577 (1992).
52. Weigend, F. & Ahlrichs, R. Balanced basis sets of split valence, triple zeta valence and quadruple zeta valence quality for H to Rn: Design and assessment of accuracy. *Phys. Chem. Chem. Phys.* **7**, 3297–3305 (2005).
53. Wang, J., Wolf, R. M., Caldwell, J. W., Kollman, P. A. & Case, D. A. Development and testing of a general amber force field. *J. Comput. Chem.* **25**, 1157–1174 (2004).
54. Plimpton, S. Fast parallel algorithms for short-range molecular dynamics. *J. Comput. Phys.* **117**, 1-19 (1995)
55. Shirts, M. R. & Chodera, J. D. Statistically optimal analysis of samples from multiple equilibrium states. *J. Chem. Phys.* **129**, 124105 (2008).

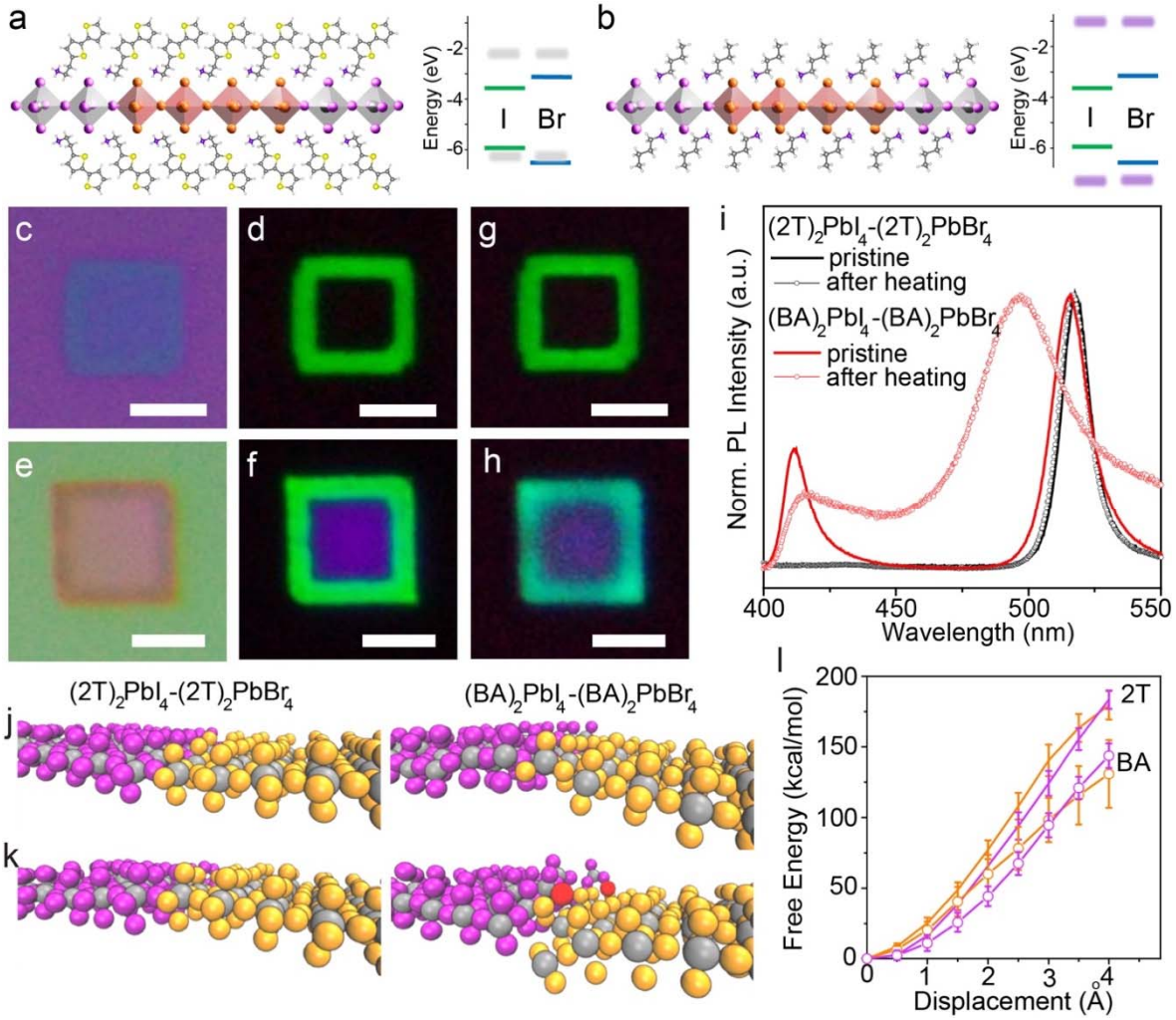

Fig. 1 | Two-dimensional halide perovskite lateral heterostructures stabilized by conjugated ligands. Schematic illustrations and proposed band alignments of **a,** $(2T)_2PbI_4$-$(2T)_2PbBr_4$ and **b,** $(BA)_2PbI_4$-$(BA)_2PbBr_4$ lateral heterostructures. The blue and green lines represent the conduction band minimum (CBM) and valence band maximum (VBM) of inorganic $[PbBr_4]^{2-}$ and $[PbI_4]^{2-}$ octahedral layers, respectively. The broad and semi-transparent grey and purple lines correspond to the highest occupied molecular orbital (HOMO) and lowest unoccupied molecular orbital (LUMO) levels of $2T^+$ and BA^+organic layers, respectively. **c, d,** Optical and PL images of a $(2T)_2PbI_4$-$(2T)_2PbBr_4$ lateral heterostructure. **e, f,** Optical and PL images of a $(BA)_2PbI_4$-$(BA)_2PbBr_4$ lateral heterostructure. **g,** PL image of the $(2T)_2PbI_4$-$(2T)_2PbBr_4$ lateral heterostructure after 1 h of heating at 100 °C. **h,** PL image of the $(BA)_2PbI_4$-$(BA)_2PbBr_4$ lateral heterostructure after 1 h of heating at 100 °C. All scale bars are 3 μm. **i,** Corresponding PL spectra of the heterostructures before and after heating. Snapshots from the molecular dynamics simulations at 298 K **(j)** and 800 K **(k)** for $(BA)_2PbI_4$-$(BA)_2PbBr_4$ (right) and $(2T)_2PbI_4$-$(2T)_2PbBr_4$ (left) showing the interface between each perovskite domain. For clarity, the organic ligands have been omitted. The colors correspond to: purple for iodine atoms, orange for bromine atoms, and gray for lead atoms. The iodine atoms that have diffused across the interface in $(BA)_2PbI_4$-$(BA)_2PbBr_4$ and into the bromine domain are indicated by the color red. **l,** Free energy of removing a halide atom from an apical position to vacuum to generate a halide vacancy. Orange plots correspond to bromide perovskite and purple plots correspond to iodide perovskites.

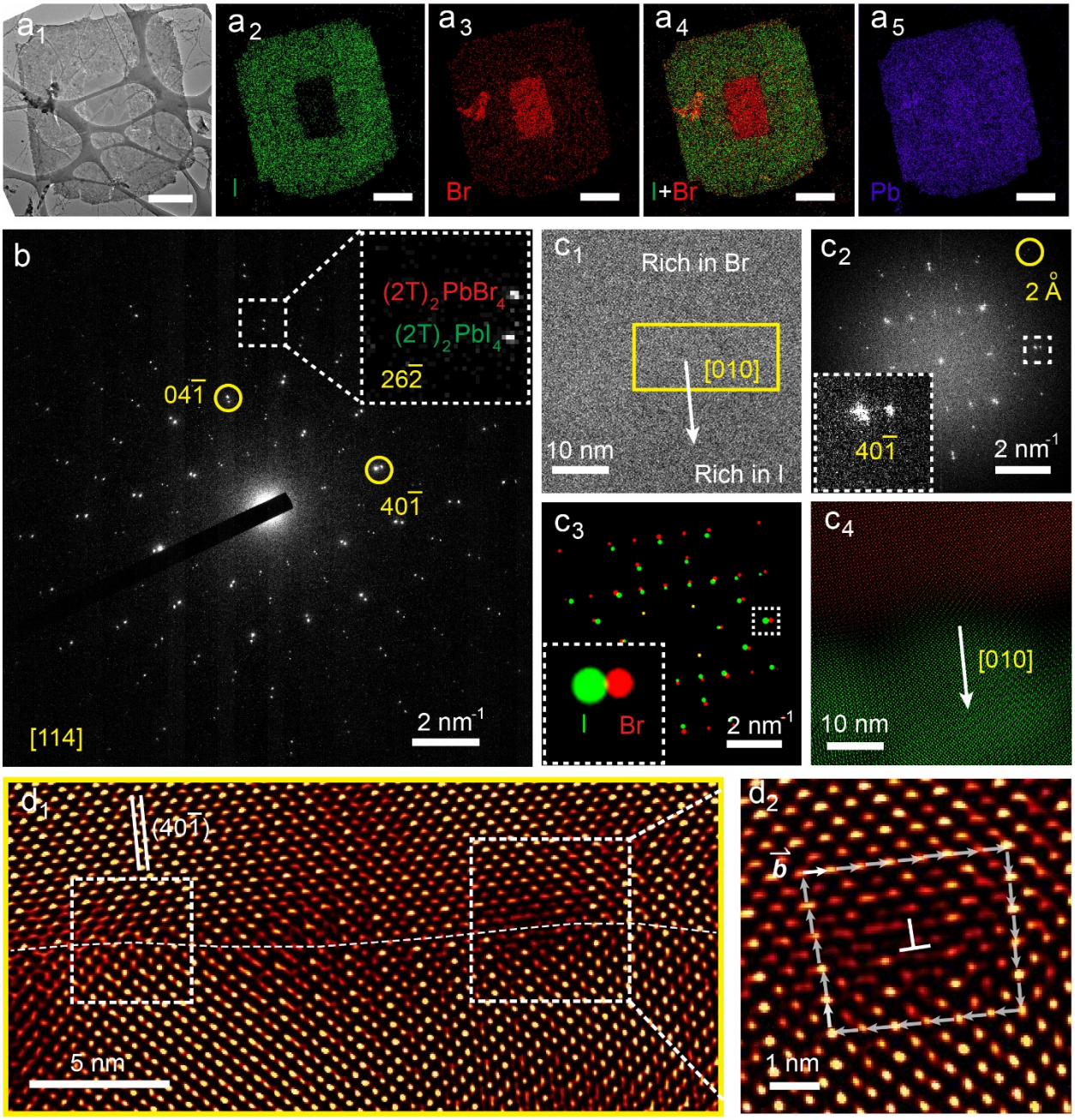

Fig. 2 | TEM characterization of the $(2T)_2PbI_4$-$(2T)_2PbBr_4$ heterostructure. a, Low-magnification TEM image (**a**$_1$) and EDS elemental mappings of one $(2T)_2PbI_4$-$(2T)_2PbBr_4$ heterostructure, where (**a**$_2$**, a**$_3$**,** $\mathbf{a}_4$ and $\mathbf{a}_5$) represent the elemental mapping of I, Br, I + Br, and Pb, respectively. The scale bars are 1 μm. **b,** SAED pattern of the $(2T)_2PbI_4$-$(2T)_2PbBr_4$ interface. Inset is the enlarged view of one pair of splitting diffraction spots. The zone axis is [114]; **c,** AC-HRTEM and Fourier analysis. $\mathbf{c}_1$, A selected AC-HRTEM image. $\mathbf{c}_2$, ~~F~~FFT pattern. One pair of splitting spots is enlarged. $\mathbf{c}_3$, False-colored Fourier masks for two sets of spots. One pair of masks for splitting spots is enlarged. $\mathbf{c}_4$, Corresponding overlap of two sets of lattice fringes from $(2T)_2PbI_4$ and $(2T)_2PbBr_4$, respectively. False color is used to clearly distinguish $(2T)_2PbI_4$ from $(2T)_2PbBr_4$. $\mathbf{d}_1$, Fourier filtered and magnified AC-HRTEM image showing the epitaxial interface. $\mathbf{d}_2$, Enlarged image of an edge dislocation. The white arrow denotes the Burger vector $\vec{b}$.

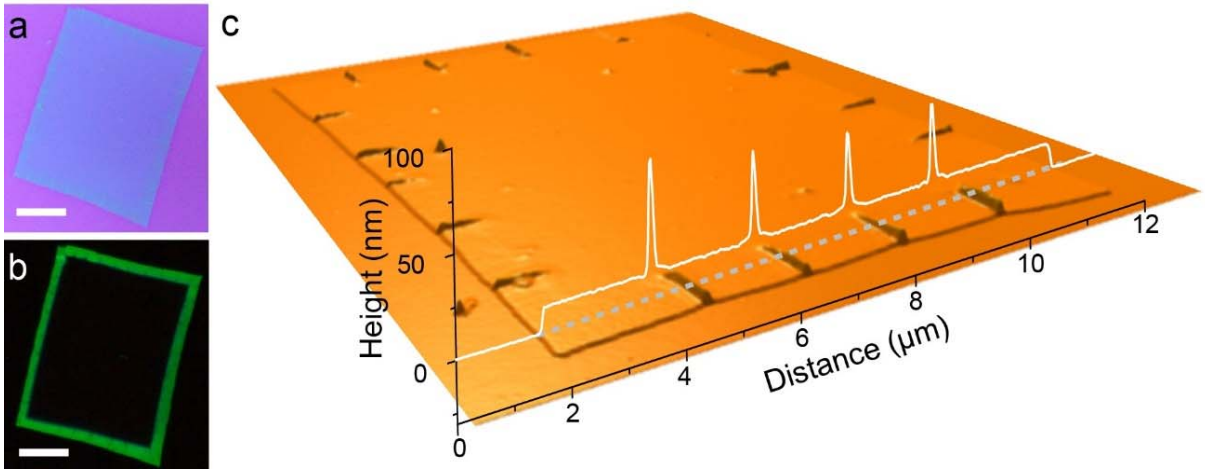

Fig. 3 | Periodic ripples in $(2T)_2PbI_4$-$(2T)_2PbBr_4$ lateral heterostructures. a, b, Optical and PL images of a one-pot $(2T)_2PbI_4$-$(2T)_2PbBr_4$ lateral heterostructure, where ripples in the $(2T)_2PbI_4$ region can be distinguished. The scale bars are 5 μm. **c,** AFM image of the one-pot $(2T)_2PbI_4$-$(2T)_2PbBr_4$ lateral heterostructure with clear ripples. The height profile along the dashed line indicates the height of the ripples is around 40~50 nm.

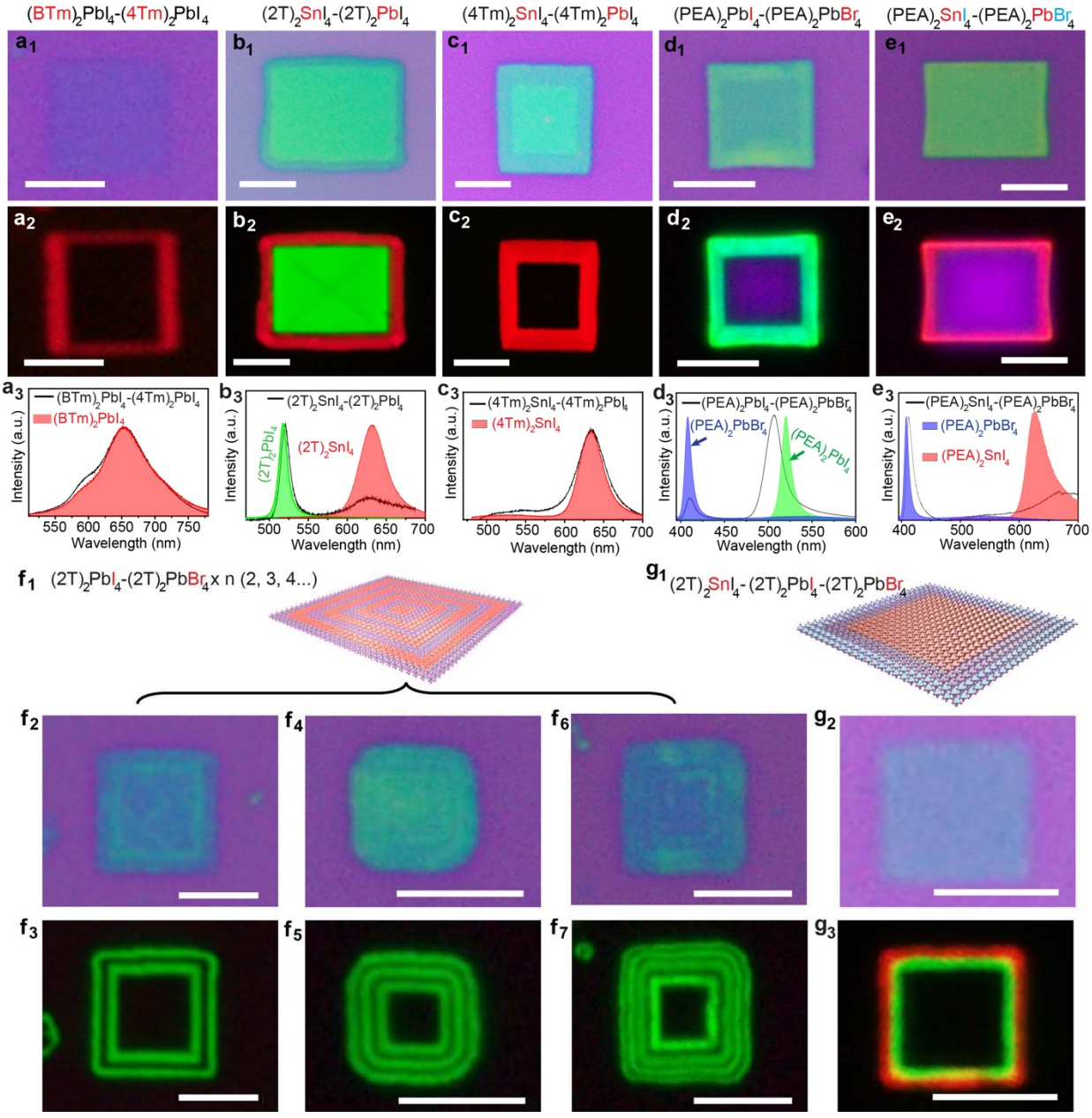

Fig. 4 | The library of 2D halide perovskite lateral heterostructures, multi-heterostructures and superlattices. **a,** $(BTm)_2PbI_4$-$(4Tm)_2PbI_4$ lateral heterostructure. **b,** $(2T)_2SnI_4$-$(2T)_2PbI_4$ lateral heterostructure. **c,** $(4Tm)_2SnI_4$-$(4Tm)_2PbI_4$ lateral heterostructure. **d,** $(PEA)_2PbI_4$-$(PEA)_2PbBr_4$ lateral heterostructure. **e,** $(PEA)_2SnI_4$-$(PEA)_2PbBr_4$ lateral heterostructure. **f,** $(2T)_2PbI_4$-$(2T)_2PbBr_4$ ×n (n=2, 3, 4) lateral superlattice. **g,** $(2T)_2SnI_4$-$(2T)_2PbI_4$-$(2T)_2PbBr_4$ lateral multi-heterostructure. **a_1, b_1, c_1, d_1, e_1, f_2, f_4, f_6, g_2** are optical images; **a_2, b_2, c_2, d_2, e_2, f_3, f_5, f_7, g_3** are PL images; **a_3, b_3, c_3, d_3, e_3** are PL spectra; **f_1, g_1** are schematic illustrations. Scale bars for **(a)** and **(g)** are 3 μm. All other scale bars are 5 μm.

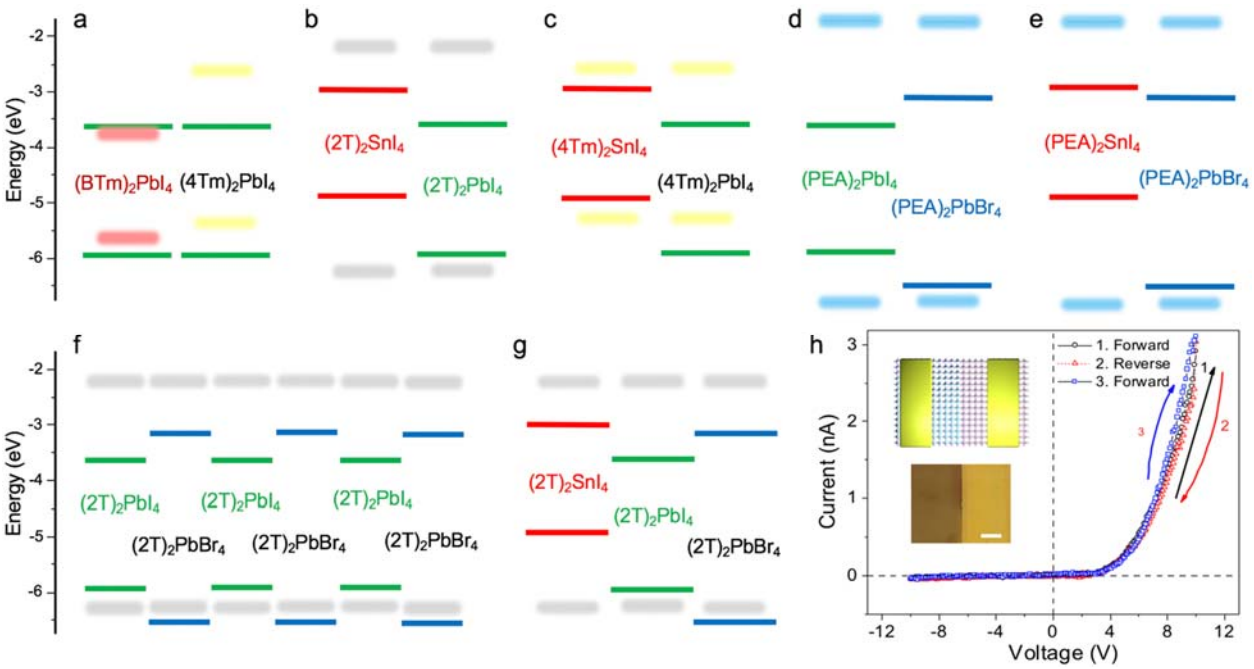

Fig. 5 | Proposed band alignments and electrical characteristics of the heterostructures. **a-g,** $(BTm)_2PbI_4$-$(4Tm)_2PbI_4$ (**a**), $(2T)_2SnI_4$-$(2T)_2PbI_4$ (**b**), $(4Tm)_2SnI_4$-$(4Tm)_2PbI_4$ (**c**), $(PEA)_2PbI_4$-$(PEA)_2PbBr_4$ (**d**), $(PEA)_2SnI_4$-$(PEA)_2PbBr_4$ (**e**), $(2T)_2PbI_4$-$(2T)_2PbBr_4$ × 3 superlattices (**f**), $(2T)_2SnI_4$-$(2T)_2PbI_4$-$(2T)_2PbBr_4$ (**g**). The blue, green and red lines represent the CBM and VBM of inorganic $[PbBr_4]^{2-}$, $[PbI_4]^{2-}$, and $[SnI_4]^{2-}$ octahedral layers, respectively. The broad and semi-transparent grey, red, yellow and blue lines correspond to the HOMO and LUMO of $2T^+$, BTm^+, $4Tm^+$ and PEA^+ organic layers; respectively. Band bending and fermi level matching is not considered as these values have not yet been reliably measured and reported. **h,** Rectification behavior of a $(4Tm)_2SnI_4$-$(4Tm)_2PbI_4$ heterostructure diode device. Inset, schematic illustration and optical image of the thin-film $(4Tm)_2SnI_4$-$(4Tm)_2PbI_4$ heterostructure. The scale bar is 2 mm.

Supplementary Information for

Two-Dimensional Halide Perovskite Lateral Epitaxial Heterostructures

Enzheng Shi, Biao Yuan, Stephen B. Shiring, Yao Gao, Akriti, Yunfan Guo, Cong Su, Minliang Lai, Peidong Yang, Jing Kong, Brett M. Savoie*, Yi Yu*, Letian Dou*

*Corresponding author. E-mail: dou10@purdue.edu (L.D.); yuyi1@shanghaitech.edu.cn (Y.Y.); bsavoie@purdue.edu (B.M.S.)

Supplementary Text and Figures

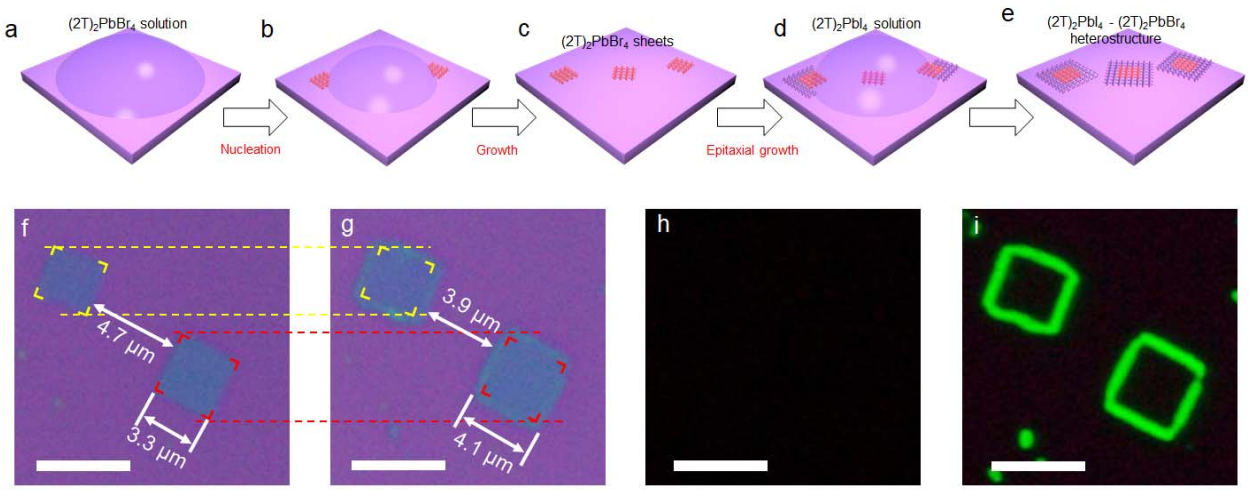

Supplementary Fig. 1 | Epitaxial growth of $(2T)_2PbI_4$-$(2T)_2PbBr_4$ lateral heterostructures. **a-e**, Flow diagram showing the epitaxial growth of $(2T)_2PbI_4$-$(2T)_2PbBr_4$ heterostructures. **a,** Adding 10 μL of $(2T)_2PbBr_4$ precursor solution to grow $(2T)_2PbBr_4$ sheets. **b,** Nucleation of $(2T)_2PbBr_4$ sheets with the evaporation of the co-solvents. **c**, Formation of $(2T)_2PbBr_4$ sheets on the substrate after all co-solvents evaporate. **d**, Adding 10 μL of diluted $(2T)_2PbI_4$ precursor solution for the epitaxial growth of $(2T)_2PbI_4$ from the existing $(2T)_2PbBr_4$ sheets. **e**, After the co-solvents evaporate, $(2T)_2PbI_4$- $(2T)_2PbBr_4$ heterostructures are formed on the substrate. The growth of other types of 2D lateral halide perovskite heterostructures follows the same procedures. For clarity, the organic ligands have been omitted. **f**, Optical image of two $(2T)_2PbBr_4$ sheets grown on SiO_2/Si substrates. **g**, Optical image of $(2T)_2PbBr_4$ -$(2T)_2PbI_4$ heterostructures after epitaxial growth of $(2T)_2PbI_4$ from the existing $(2T)_2PbBr_4$ sheets. The dashed yellow and red frames indicate the outline of $(2T)_2PbBr_4$ sheets. The separation between these two square sheets was 4.7 μm initially and narrowed down to 3.9 μm after heterostructure formation. Meanwhile, the lateral length of right sheet was 3.3 μm and increased to 4.1 μm after the heterostructure formation. Above results rule out the possibility of ion exchange mechanism and further validates the epitaxial growth mechanism for 2D halide perovskite lateral heterostructures. **h, i**, Corresponding PL images of $(2T)_2PbBr_4$ sheets and $(2T)_2PbBr_4$ -$(2T)_2PbI_4$ heterostructures. The scale bars are 5 μm.

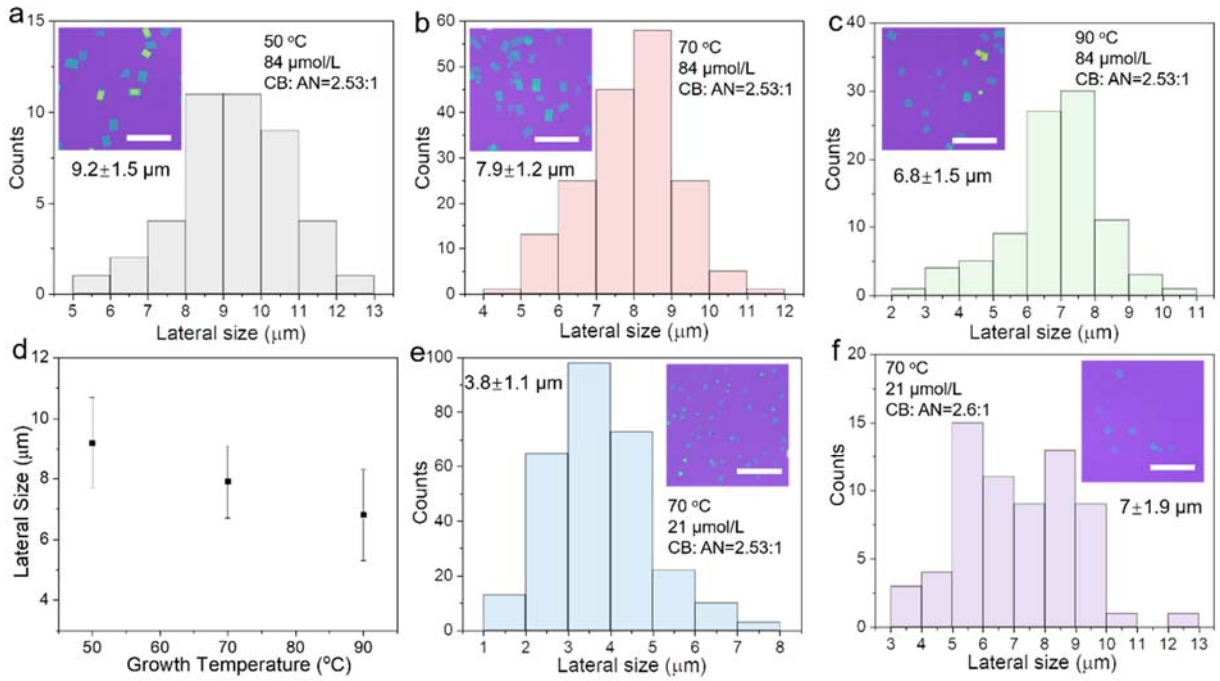

Supplementary Fig. 2 | Lateral size control of $(2T)_2PbBr_4$ sheets. **a-c,** Statistics of lateral size of $(2T)_2PbBr_4$ sheets grown at 50, 70 and 90 °C, respectively. The precursor solution concentration is 84 μmol/L, and the CB: AN ratio is 2.53:1. **d**, Dependence of $(2T)_2PbBr_4$ lateral size on the growth temperature. **e**, Statistics of lateral size of $(2T)_2PbBr_4$ sheets grown from 21 μmol/L of precursor solution. The growth temperature is 70 °C, and the CB: AN ratio is 2.53:1. **f**, Statistics of lateral size of $(2T)_2PbBr_4$ sheets grown from precursor solution with CB:AN ratio of 2.6:1. The growth temperature is 70 °C, and the precursor solution concentration is 21 μmol/L. Insets: representative optical images of $(2T)_2PbBr_4$ sheets grown under corresponding conditions. The scale bars are 50 μm.

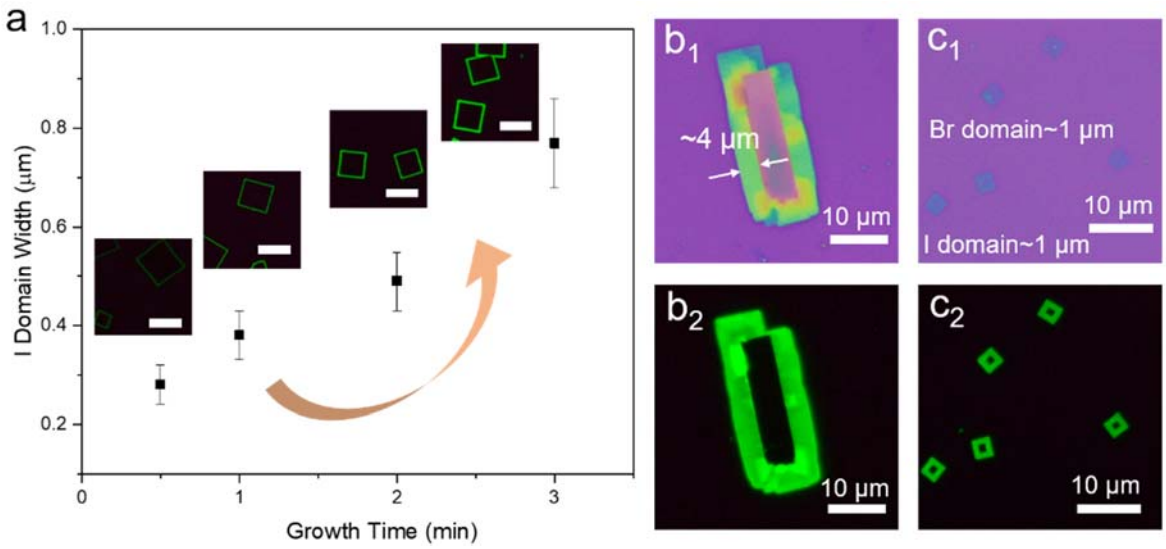

Supplementary Fig. 3 | Lateral size control of $(2T)_2PbI_4$ domain in $(2T)_2PbI_4$-$(2T)_2PbBr_4$ lateral heterostructures. a, The lateral size of $(2T)_2PbI_4$ domains with respect to the growth time. Inset PL images indicate the evolution of heterostructures with the increase of growth time. The scale bars are 10 μm. **b**, One $(2T)_2PbI_4$-$(2T)_2PbBr_4$ lateral heterostructure with 4 μm wide $(2T)_2PbI_4$ domain. **c**, $(2T)_2PbI_4$-$(2T)_2PbBr_4$ lateral heterostructures with optimized lateral sizes. Both $(2T)_2PbI_4$ and $(2T)_2PbBr_4$ domains have a lateral size of ~ 1 μm.

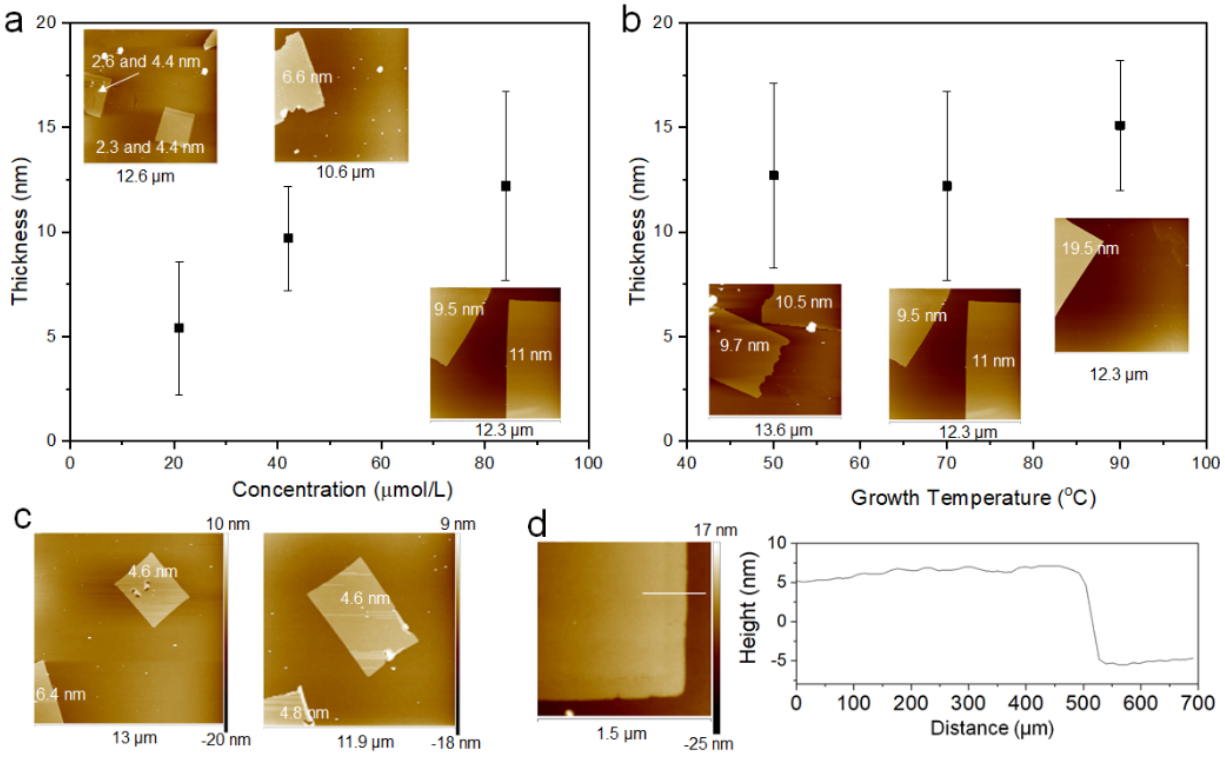

Supplementary Fig. 4 | Thickness control of $(2T)_2PbBr_4$ sheets and $(2T)_2PbI_4$-$(2T)_2PbBr_4$ lateral heterostructures. **a,** Precursor solution concentration dependence of $(2T)_2PbBr_4$ sheets thickness. Inset: representative AFM images of $(2T)_2PbBr_4$ sheets grown from 21, 42 and 84 μmol/L of solution. The growth temperature is 70 ºC, and the CB: AN ratio is 2.53:1. **b**, Growth temperature dependence of $(2T)_2PbBr_4$ sheets thickness. Inset: representative AFM images of $(2T)_2PbBr_4$ sheets grown under 50, 70 and 90 ºC respectively. The solution concentration is 84 μmol/L, and the CB: AN ratio is 2.53:1. **c,** AFM images of $(2T)_2PbBr_4$ sheets grown from precursor solution with CB: AN of 2.6: 1. The growth temperature is 70 ºC, and the solution concentration is 21 μmol/L. **d,** The AFM image and height profile of $(2T)_2PbI_4$-$(2T)_2PbBr_4$ lateral heterostructure.

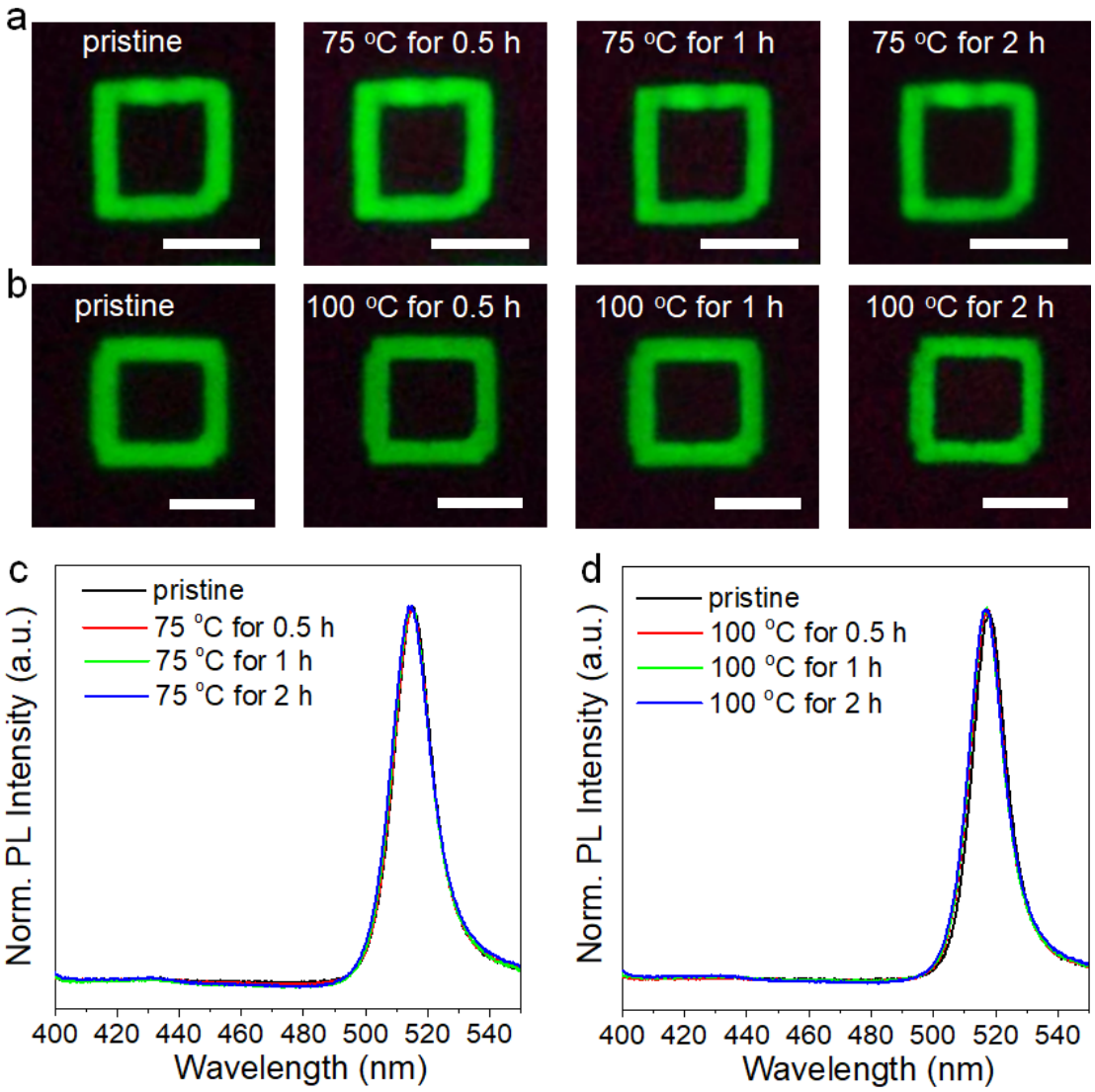

Supplementary Fig. 5 | Dynamic tracking of PL emission of $(2T)_2PbI_4$-$(2T)_2PbBr_4$ heterostructures. a, PL images of one $(2T)_2PbI_4$-$(2T)_2PbBr_4$ heterostructure at pristine state, after 0.5 h, 1 h and 2h of heating under 75 °C, respectively. **b,** PL images of another $(2T)_2PbI_4$-$(2T)_2PbBr_4$ heterostructure at pristine state, after 0.5 h, 1 h and 2h of heating under 100 °C, respectively. **c,** Corresponding PL spectra of the $(2T)_2PbI_4$-$(2T)_2PbBr_4$ heterostructure in (**a**). **d,** Corresponding PL spectra of the $(2T)_2PbI_4$-$(2T)_2PbBr_4$ heterostructure in (**b**). The stable PL emission indicates the high stability of $(2T)_2PbI_4$-$(2T)_2PbBr_4$ heterostructure under 75 and 100 °C heating and the effective inhibition of halide anion interdiffusion. All scale bars are 3 μm.

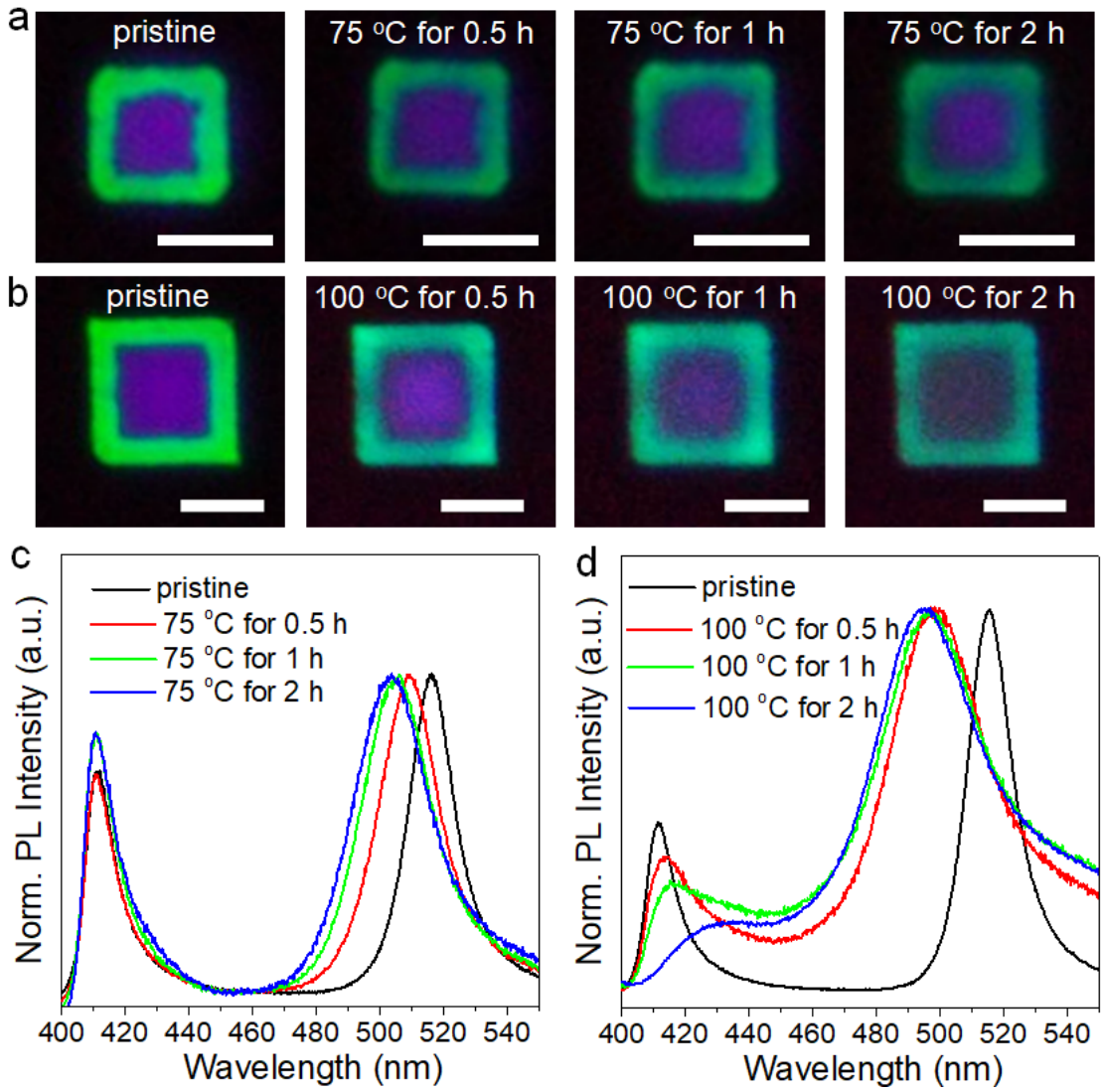

Supplementary Fig. 6 | Dynamic tracking of PL emission of $(BA)_2PbI_4$-$(BA)_2PbBr_4$ heterostructures. a, PL images of one $(BA)_2PbI_4$-$(BA)_2PbBr_4$ heterostructure at pristine state, after 0.5 h, 1 h and 2h of heating under 75 °C, respectively. **b,** PL images of another $(BA)_2PbI_4$-$(BA)_2PbBr_4$ heterostructure at pristine state, after 0.5 h, 1 h and 2h of heating under 100 °C, respectively. **c,** Corresponding PL spectra of the $(BA)_2PbI_4$-$(BA)_2PbBr_4$ heterostructure in (**a**). **d,** Corresponding PL spectra of the $(BA)_2PbI_4$-$(BA)_2PbBr_4$ heterostructure in (**b**). The significant shift of the PL emission indicates the halide interdiffusion under 75 and 100 °C heating. All scale bars are 3 μm.

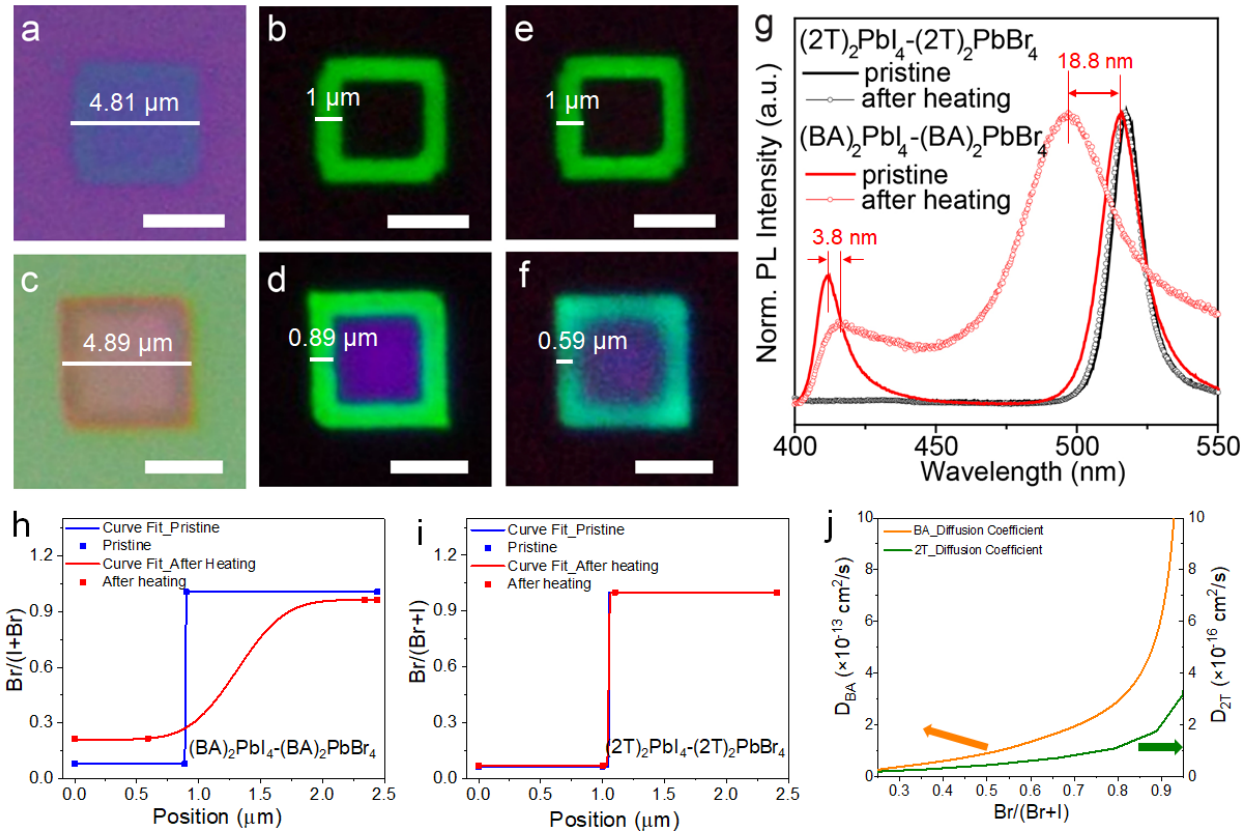

Supplementary Fig. 7 | Diffusion Coefficient calculation for BA and 2T lateral heterostructures. a, b, Optical and PL images of a $(2T)_2PbI_4$-$(2T)_2PbBr_4$ lateral heterostructure. **c, d,** Optical and PL images of a $(BA)_2PbI_4$-$(BA)_2PbBr_4$ lateral heterostructure. **e,** PL image of the $(2T)_2PbI_4$-$(2T)_2PbBr_4$ lateral heterostructure after 1 h of heating at 100 ºC. **f,** PL image of the $(BA)_2PbI_4$-$(BA)_2PbBr_4$ lateral heterostructure after 1 h of heating at 100 ºC. **g,** Corresponding PL spectra of the heterostructures before and after heating. All scale bars are 3 μm. This figure is part of Fig. 1 in the main text. Experimental data and corresponding normal cumulative distribution function (CDF) fit for concentration profiles before and after heating across BA (**h**) and 2T (**i**) lateral heterostructures. **j,** Calculated inter-diffusion coefficient values for halide diffusion across for BA and 2T lateral heterostructures using Boltzmann-Matano method.

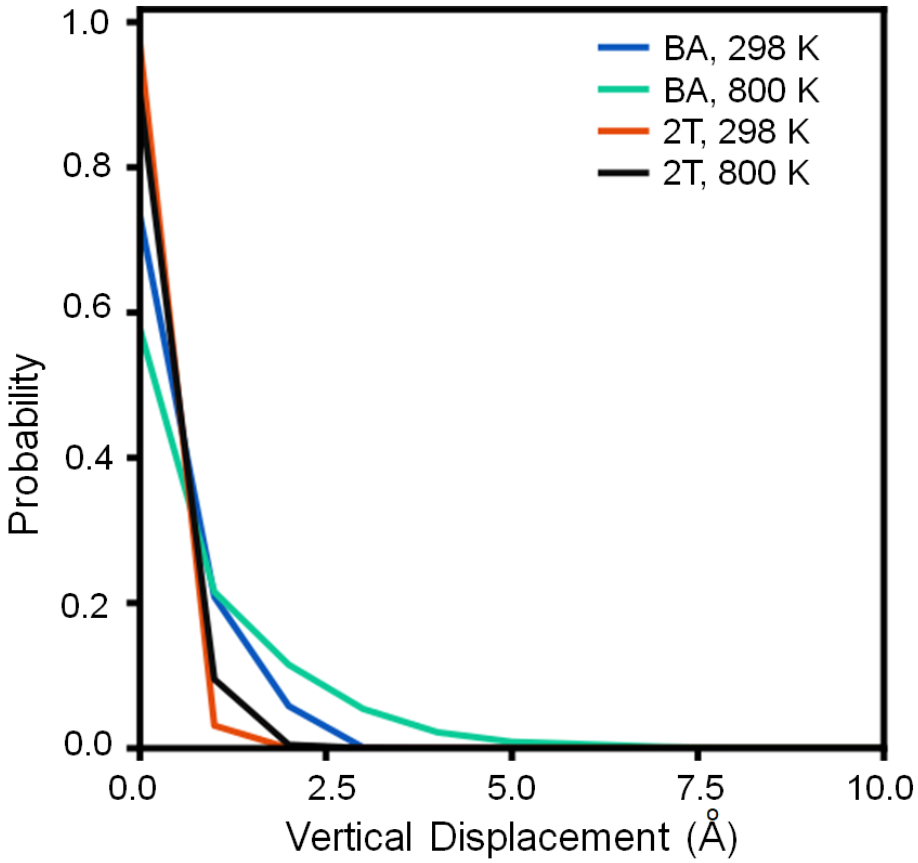

Supplementary Fig. 8 | Summary of lead atom displacements from initial ideal positions for $(BA)_2PbI_4$-$(BA)_2PbBr_4$ ("BA") and $(2T)_2PbI_4$-$(2T)_2PbBr_4$ ("2T"). The larger organic ligand (2T) leads to decreased elasticity in the inorganic framework as evidenced by the tight cluster of small displacements, both at room and elevated temperatures. The smaller organic ligand (BA) leads to a more elastic framework, which is exaggerated at the elevated temperature.

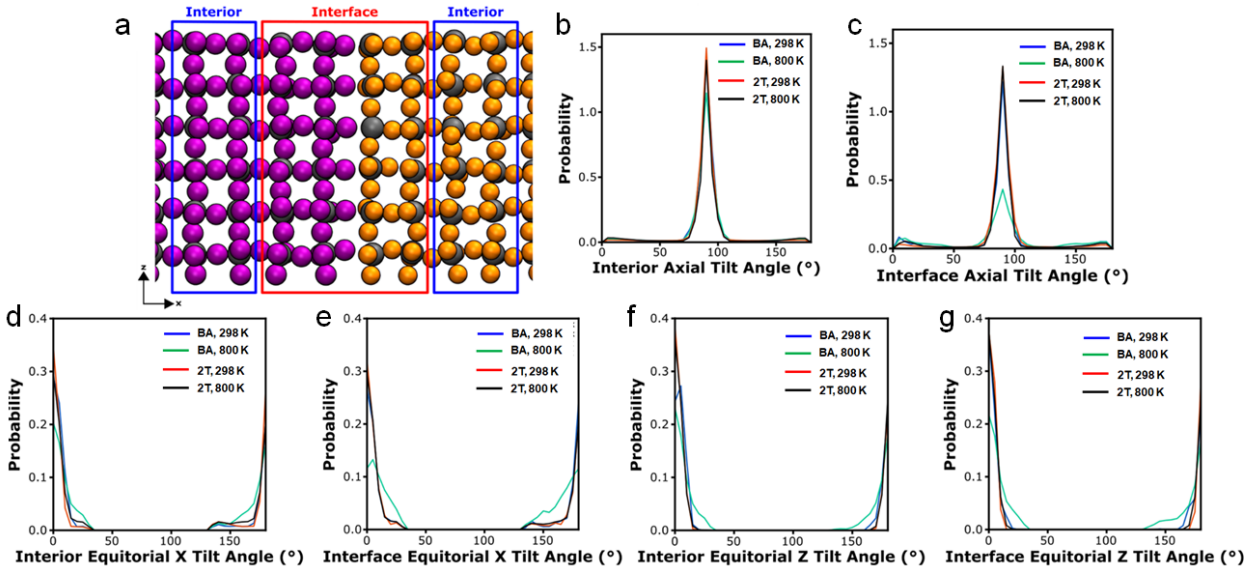

Supplementary Fig. 9 | Lead octahedron disorder as a function of location within the perovskite, quantifying the increase in disorder at the interface. a, The lead atoms were identified as belonging either to the interface or the interior, and their disorder tracked accordingly. **b-g,** Axial tilt as defined by a vector between the apical halides relative to the lead plane; for both ligands at both room and elevated temperatures, the interior lead octahedrons remain ideally perpendicular to the lead plane. Although the interface is disordered with both ligands at room temperature, BA is less capable in stabilizing the interface, leading to an increase in interfacial disorder at elevated temperatures. For the equatorial tilt, the tilt out of the lead plane was partitioned into the x and z components, with the x direction perpendicular to the interface and the z direction parallel to the interface. In both directions, the interface with the smaller ligand shows an increased disorder, particularly at elevated temperature. x direction shows increased disorder in case of BA ligand due to the strain induced by lattice mismatch.

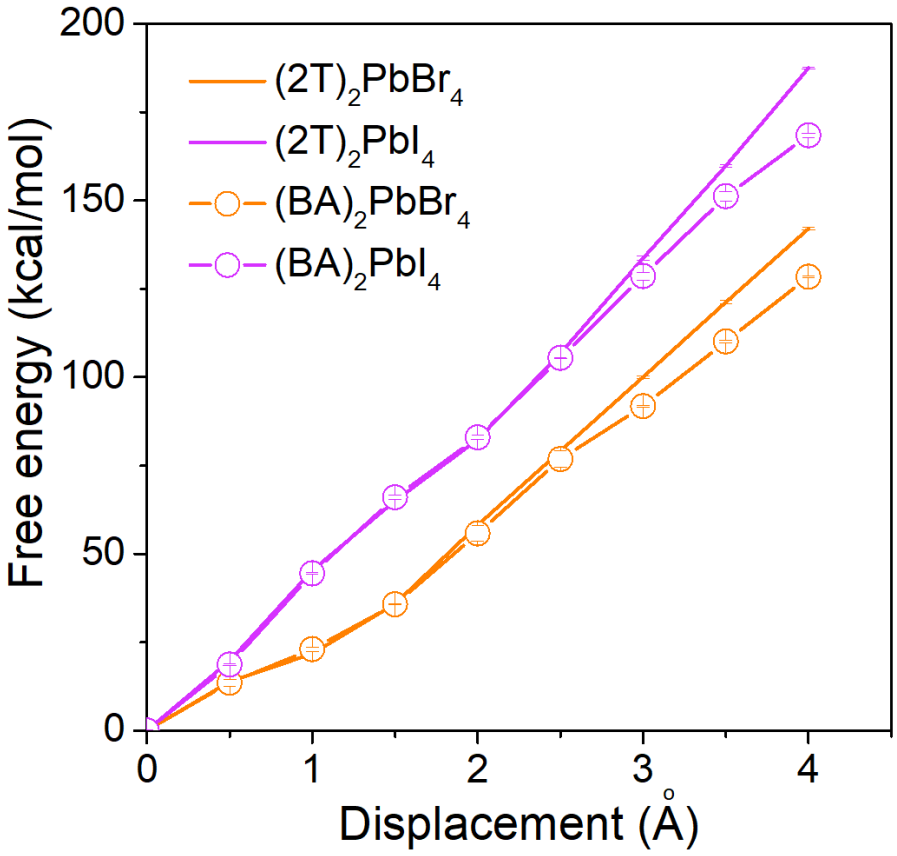

Supplementary Fig. 10 | Free energy of organic ligand vacancy formation. For a given perovskite framework, the free energy required to form a ligand vacancy is similar for BA and 2T. The number of ligand vacancies for a given perovskite framework is therefore expected to be similar for both ligands.

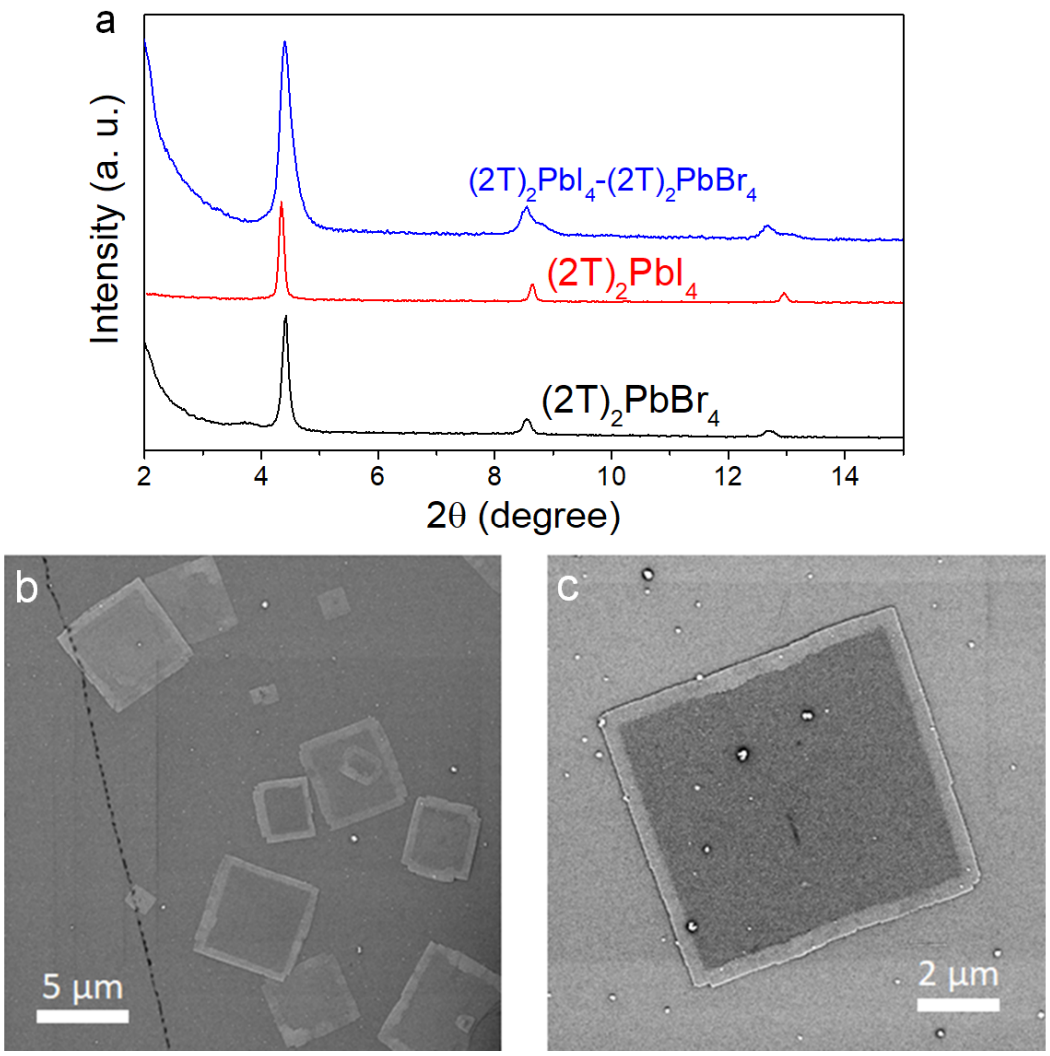

Supplementary Fig. 11 | XRD profile and SEM images of $(2T)_2PbI_4$-$(2T)_2PbBr_4$ heterostructures. a, XRD profiles of $(2T)_2PbI_4$-$(2T)_2PbBr_4$ heterostructures, pure $(2T)_2PbI_4$ and $(2T)_2PbBr_4$ sheets. Compared with the pure sheets, XRD profiles of $(2T)_2PbI_4$-$(2T)_2PbBr_4$ heterostructures have two sets of diffraction peaks, confirming that $(2T)_2PbI_4$-$(2T)_2PbBr_4$ heterostructures is composed of $(2T)_2PbI_4$ and $(2T)_2PbBr_4$ phases structurally**. b, c,** Back-scattering SEM images of $(2T)_2PbI_4$-$(2T)_2PbBr_4$ heterostructures. The elements at brighter peripheral regions (I) are heavier than those at the interior regions (Br), which is consistent with the PL and TEM characterizations.

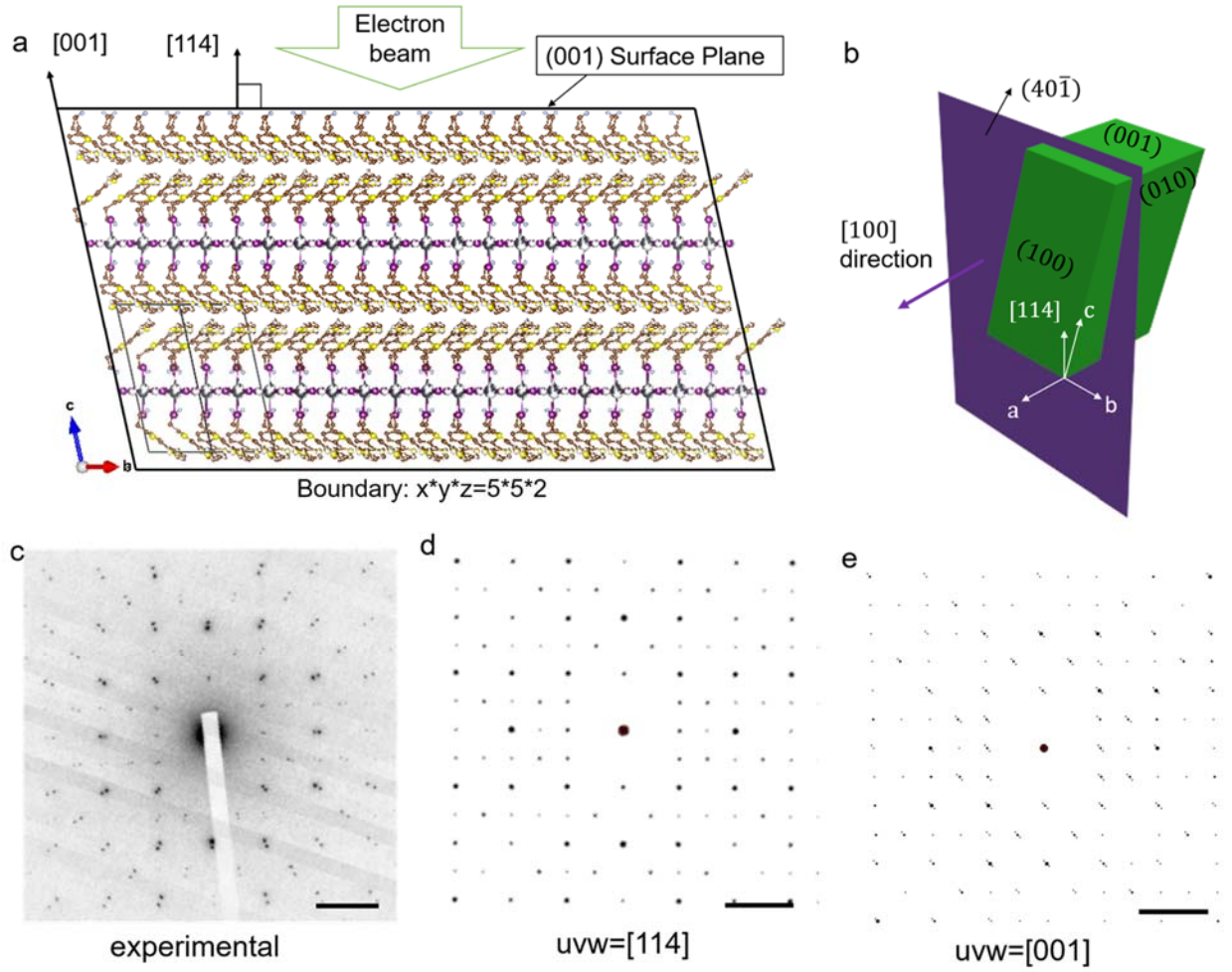

Supplementary Fig. 12 | Determination of the zone axis. a, Crystal structure of $(2T)_2PbI_4$ in [2$\bar{2}$0] projection. **b,** Schematic diagram of triclinic $(2T)_2PbI_4$ cut by (40$\bar{1}$) plane. **c,** Experimental diffraction patterns of the $(2T)_2PbI_4$-$(2T)_2PbBr_4$ heterostructure. **d, e,** Kinematical SAD patterns corresponding to uvw=[114] and uvw=[001], respectively.

By comparing the experimental diffraction patterns with kinematical SAD patterns, the simulated pattern corresponding to uvw=[114] (Supplementary Fig. 12d) is more consistent with the experimental diffraction pattern (Supplementary Fig. 12c). Since the diffraction spots of epitaxial $(2T)_2PbI_4$ and $(2T)_2PbBr_4$ come in pairs, we assume they possess similar structure and therefore we index the diffraction spots following the CIF file of $(2T)_2PbI_4$. The scale bars are 2 nm^{-1}.

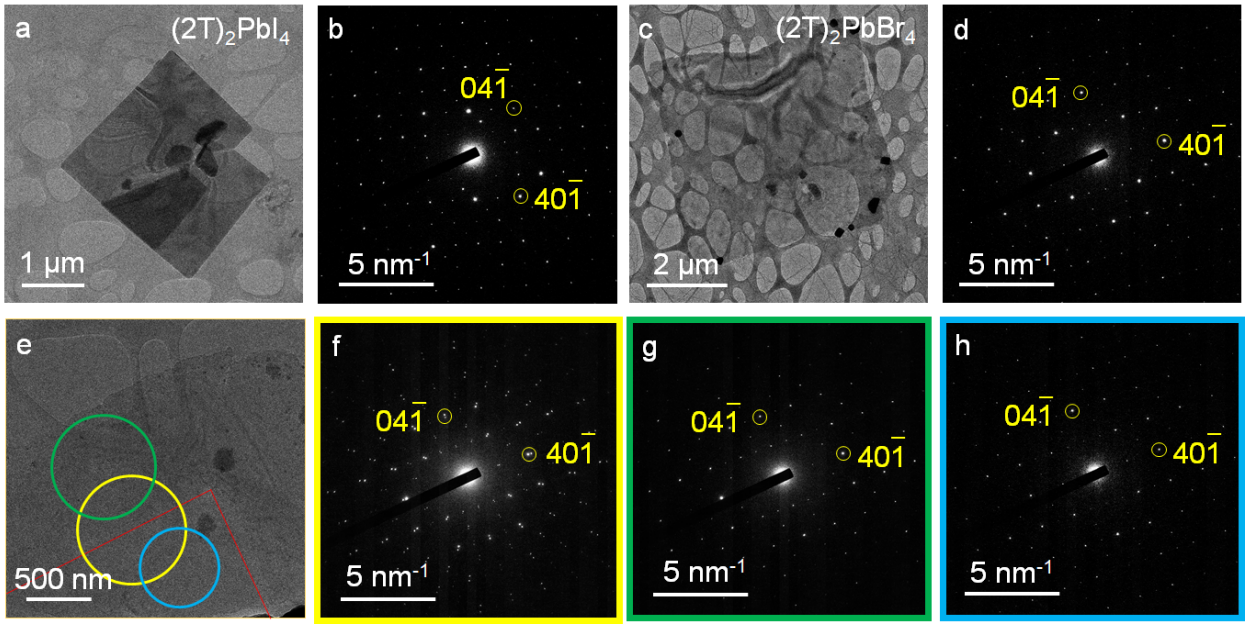

Supplementary Fig. 13 | SAED analysis of pure $(2T)_2PbI_4$, pure $(2T)_2PbBr_4$ sheets, and $(2T)_2PbI_4$-$(2T)2PbBr_4$ heterostructure. Morphology (**a**) and SAED patterns (**b**) of a pure $(2T)_2PbI_4$ sheet. Morphology (**c**) and SAED patterns (**d**) of a pure $(2T)_2PbBr_4$ sheet. Morphology (**e**) and SAED patterns (**f**) of a $(2T)_2PbI_4$-$(2T)2PbBr_4$ heterostructure. **g, h,** SAED patterns corresponding to epitaxial $(2T)_2PbI_4$ region (green circled area in E) and $(2T)_2PbBr_4$ (blue circled area in E) region, respectively.

The lattice misfits calculated from SAED patterns of pure $(2T)_2PbI_4$ and $(2T)_2PbBr_4$ (Supplementary Fig. 13b, d) are:

$$[010]f = \frac{[a(film) - a(substrate)]}{a(substrate)} = 5.9\%$$

$$[100]f = \frac{[a(film) - a(substrate)]}{a(substrate)} = 5.7\%$$

The actual lattice misfits calculated from SAED pattern of the heterostructure (Supplementary Fig. 13f) are:

$$[010]f = \frac{[a(film) - a(substrate)]}{a(substrate)} = 4.8\%$$

$$[100]f = \frac{[a(film) - a(substrate)]}{a(substrate)} = 5.0\%$$

The experimental lattice misfits calculated from ~~F~~FFT pattern of AC-HRTEM (Fig. 2b) are:

$$[010]f = \frac{[a(film) - a(substrate)]}{a(substrate)} = 5.4\%$$

$$[100]f = \frac{[a(film) - a(substrate)]}{a(substrate)} = 5.9\%$$

The slight difference in lattice misfit may be related with the lattice relaxation of 2D sheets compared to the theoretical bulk values and small amounts of Br atoms mixed in the epitaxial $(2T)_2PbI_4$.

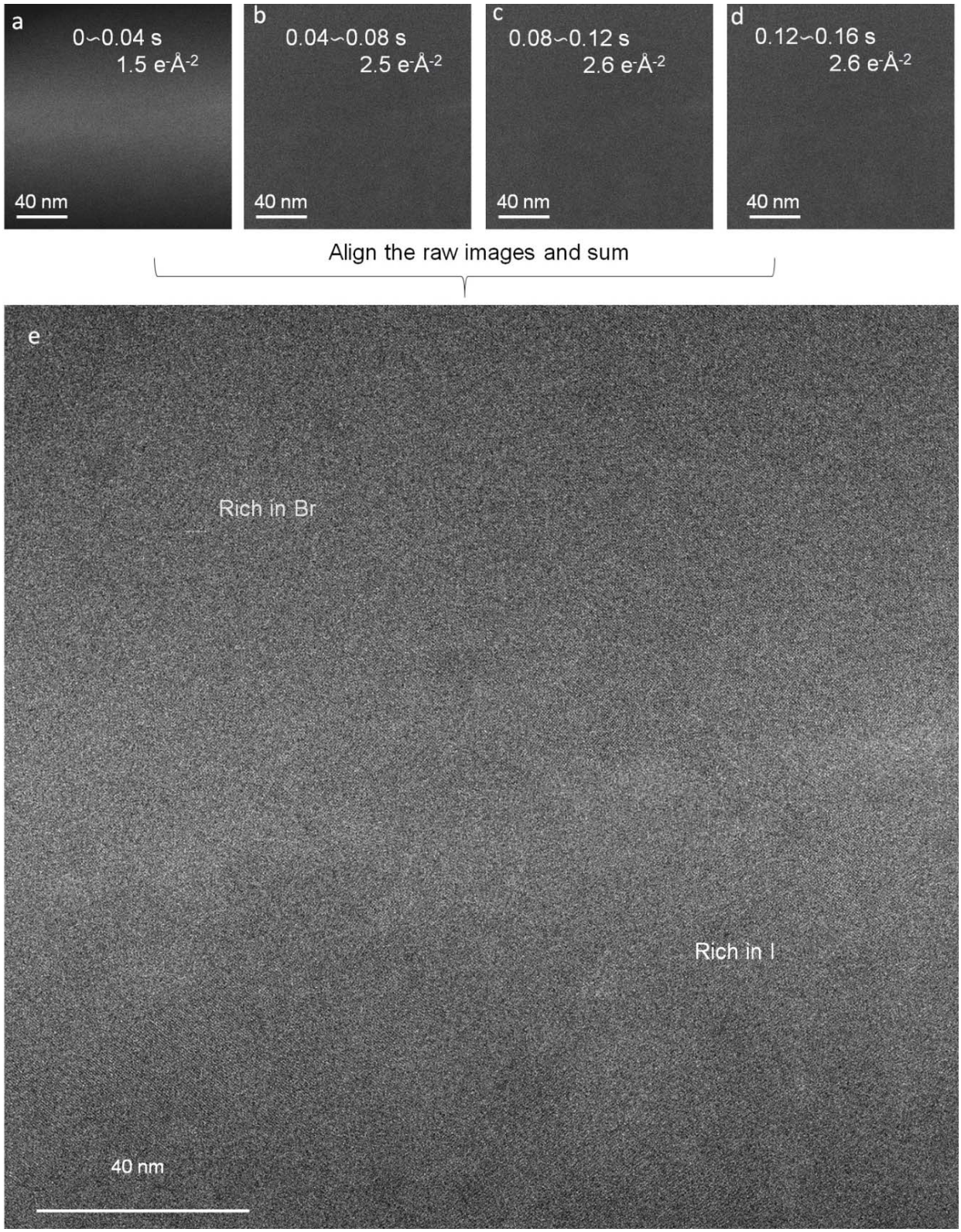

Supplementary Fig. 14 | AC-HRTEM image acquisition and processing. a-d, First four images from a series of AC-HRTEM images (40 ms of exposure time for each) acquired at low dose-rate of ~65 $e^{-}Å^{-2}s^{-1}$. By comparing the first four images and their FT patterns, there is no apparent

damage under electron beam irradiation so they can be summed up to achieve higher signal-to-noise ratio. **e,** Final AC-HRTEM images summed up from above four images (**a-d**) after drift alignment. The drift is corrected by cross correlation. The total electron dose is about 9.2 $e^{-}Å^{-2}$.

The organic-inorganic halide perovskites are extremely sensitive to electrons, and more vulnerable than other well-known covalently bonded 2D materials such as graphene and transition metal dichalcogenides, as the inorganic layers and the organic layers are bonded by weak van der Waals force. Therefore, it is very challenging to acquire completely intact structure, and the experiments show that the sample will be damaged within 1 s even though the dose rate is reduced to ~65 $e\text{-}Å^{-2}s^{-1}$. In order to obtain nearly intact structure information, the electron exposure dose before acquisition need to be reduced as low as possible. However, based on our experiences of imaging beam-sensitive perovskites[1-4], it is not enough to just simply reduce the electron beam while imaging extremely sensitive materials, as any casual pre-exposure might be detrimental to the crystal structure. Here, we use a minimum dose system (MDS) to decrease the electron dose during searching and focusing the sample. Specifically, the dose rate is below 0.1 $e\text{-}Å^{-2}s^{-1}$ when searching for the region of interest (ROI), and the damage of the ROI by electron exposure is minimized because the defocus adjustment for HRTEM is done by imaging on the adjacent area, not directly on the ROI. In this case, the ROI only receives effective doses for HRTEM imaging. This is the key point of MDS. Thus, we could acquire a series of continuous exposure images when the nearly intact ROI is exposed by the relatively high dose-rate electron beam. Since the perovskites are extremely sensitive to electrons and the ROI will gradually be damaged, we only select and process the images acquired before the $(04\bar{1})$ spots disappearing. Up to then, the whole structure has not been collapsed by electron beam irradiation. Among these selected images, there might be minor displacements which will decrease the spatial resolution of the image if we simply superpose them. Ultimately, with the help of DM scripts, the drift-corrected images can be superposed to obtain a HRTEM image with improved signal-to-noise ratio, as shown above.

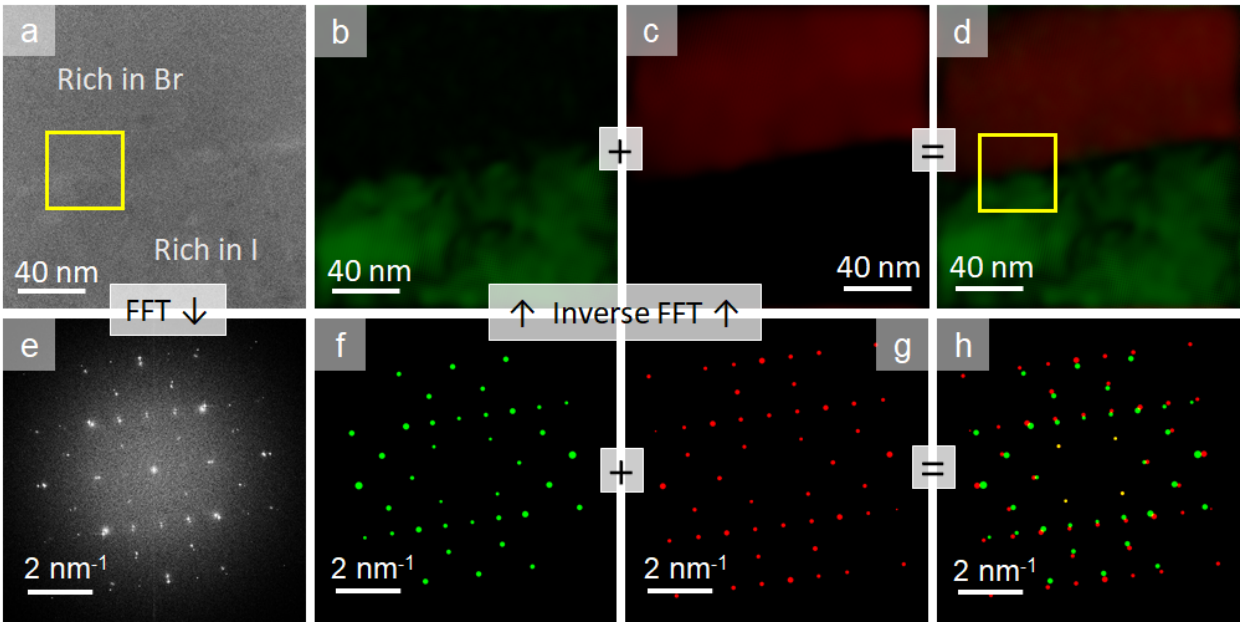

Supplementary Fig. 15 | AC-HRTEM analysis by Fourier filtering. a, AC-HRTEM image of one $(2T)_2PbI_4$-$(2T)_2PbBr_4$ heterostructure. The yellow rectangular box denotes the Fig. $2c_1$ in the main text. **b, c,** Inverse ~~F~~FTs of (**f**) and (**g**) reveal the distinct lattice information in real space respectively. **d,** Superposition of (**b**) and (**c**) shows the continuous and sharp interface. False color was used for a clear view of the interface. The yellow rectangular box denotes the Fig. $2c_4$ in the main text. **e,** ~~F~~FT pattern of (**a**). **f, g,** Two masks are placed on the diffractogram (**e**) to filter out two different phases, respectively. **h,** Superposition of (**f**) and (**g**) shows the splitting diffraction spots. False color is used for differentiating two sets of spots.

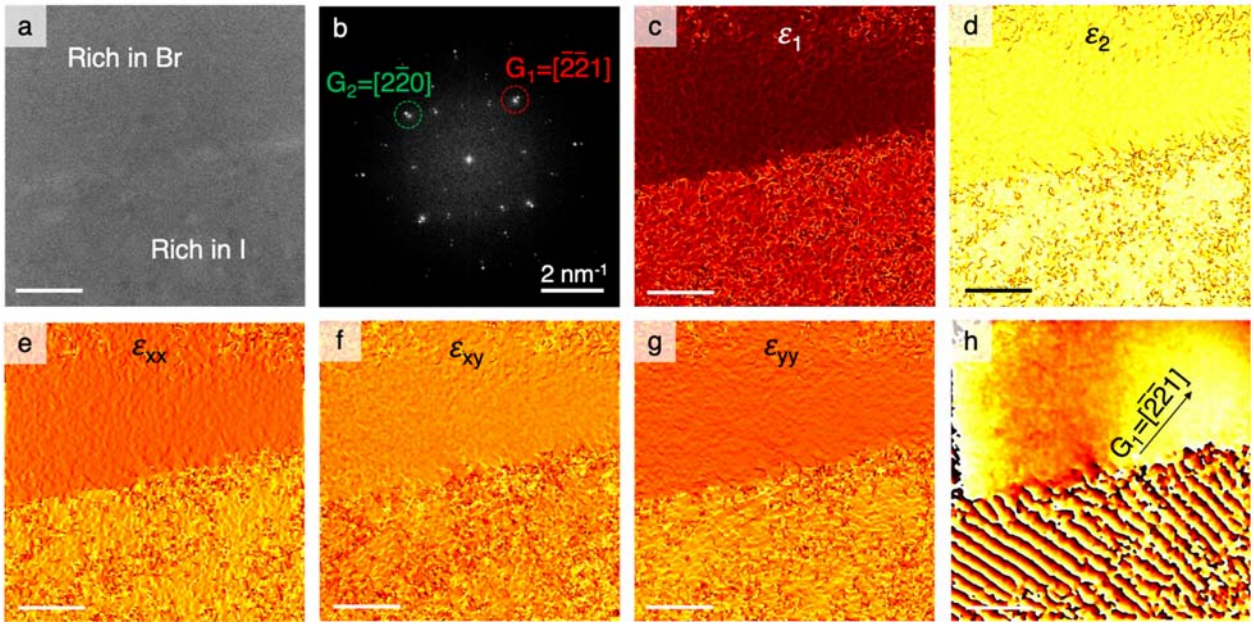

Supplementary Fig. 16 | Geometric phase analysis of the $(2T)_2PbI_4$-$(2T)_2PbBr_4$ heterostructure. a, AC-HRTEM image of the interface. **b,** ~~F~~FT pattern. $\mathbf{G_1}$ and $\mathbf{G_2}$ represents two Bragg reflections. **c,** Maximum normal strain. **d,** Minimum normal strain. **e, f, g,** Strain mappings at different directions. ε_{xx}, ε_{xy} and ε_{yy} represent the strain are parallel to the direction of Bragg reflections $\mathbf{G_1}$, $\mathbf{G_1}$+$\mathbf{G_2}$, $\mathbf{G_2}$, respectively; These strain mappings indicate the clear interface between the substrate and epitaxy. **h,** Phase image with $\mathbf{G_1}$=[$\bar{2}\bar{2}$1]. The scale bars are 40 nm. Relatively even color area shows the lattice spacing of $(2T)_2PbBr_4$ area are uniform and uneven color shows the lattice spacing of $(2T)_2PbI_4$ changes with positions regularly[5,6]. This reveals the lattice mismatch directly and implies that interfacial dislocations may exist at a certain interval to relax the lattice strain.

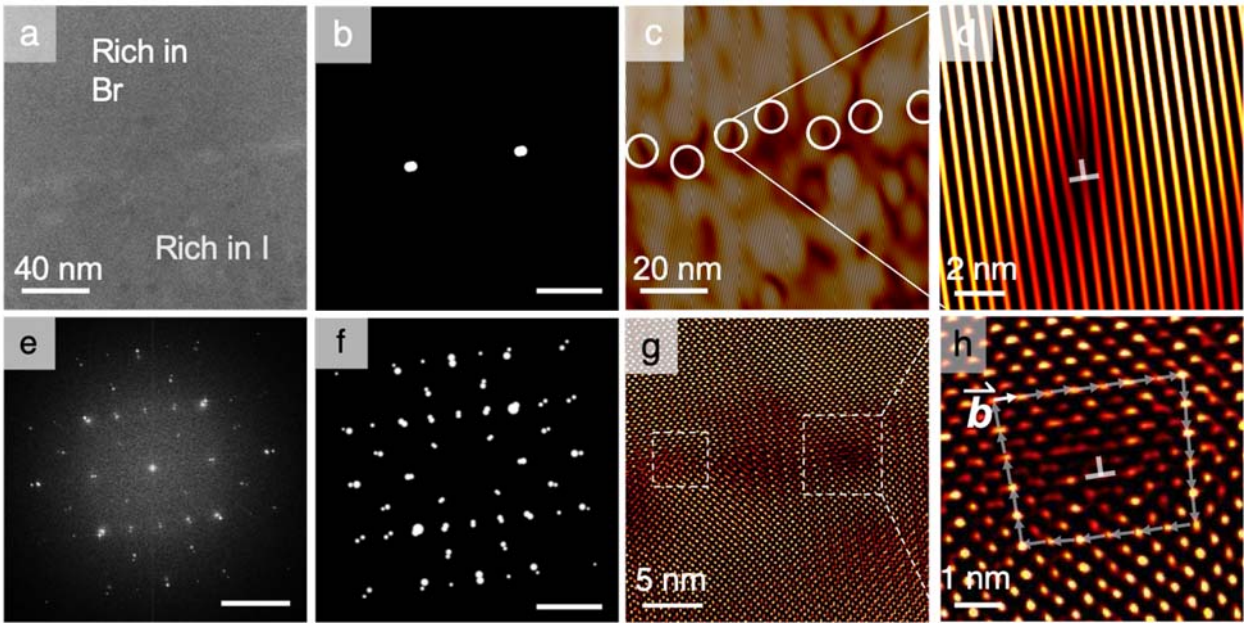

Supplementary Fig. 17 | Analysis of interfacial dislocations in the $(2T)_2PbI_4$-$(2T)_2PbBr_4$ heterostructure. a, The AC-HRTEM image. **b,** Fourier mask for two (200) spots. **c,** Magnified inverse ~~F~~FT image of (**b**) (false-colored). **d,** Magnified image shows the extra (200) plane in one of the edge dislocations. **e,** ~~F~~FT of (**a**). **f,** Fourier mask for all Bragg spots. **g,** Magnified inverse ~~F~~FT image of (**f**) (false-colored). **h,** Magnified image highlighting one of the edge dislocations.

The heteroepitaxial growth in 2D heterostructures can be maintained in 2 ways: the elastic strain is ultralow (lattice mismatch is generally within 5%, and thin epitaxial layer); the strain can be reasonably released[7,8]. To release the strain, one way is through elastic deformation of the film, which will cause a corrugated surface morphology. The other way is to form dislocation because of accumulated strain[9]. In our study, it can be directly observed that edge dislocations at the interface release strain and the epitaxial film returns to its original lattice structure periodically. The scale bars in **b**, **e** and **f** are 2 nm^{-1}.

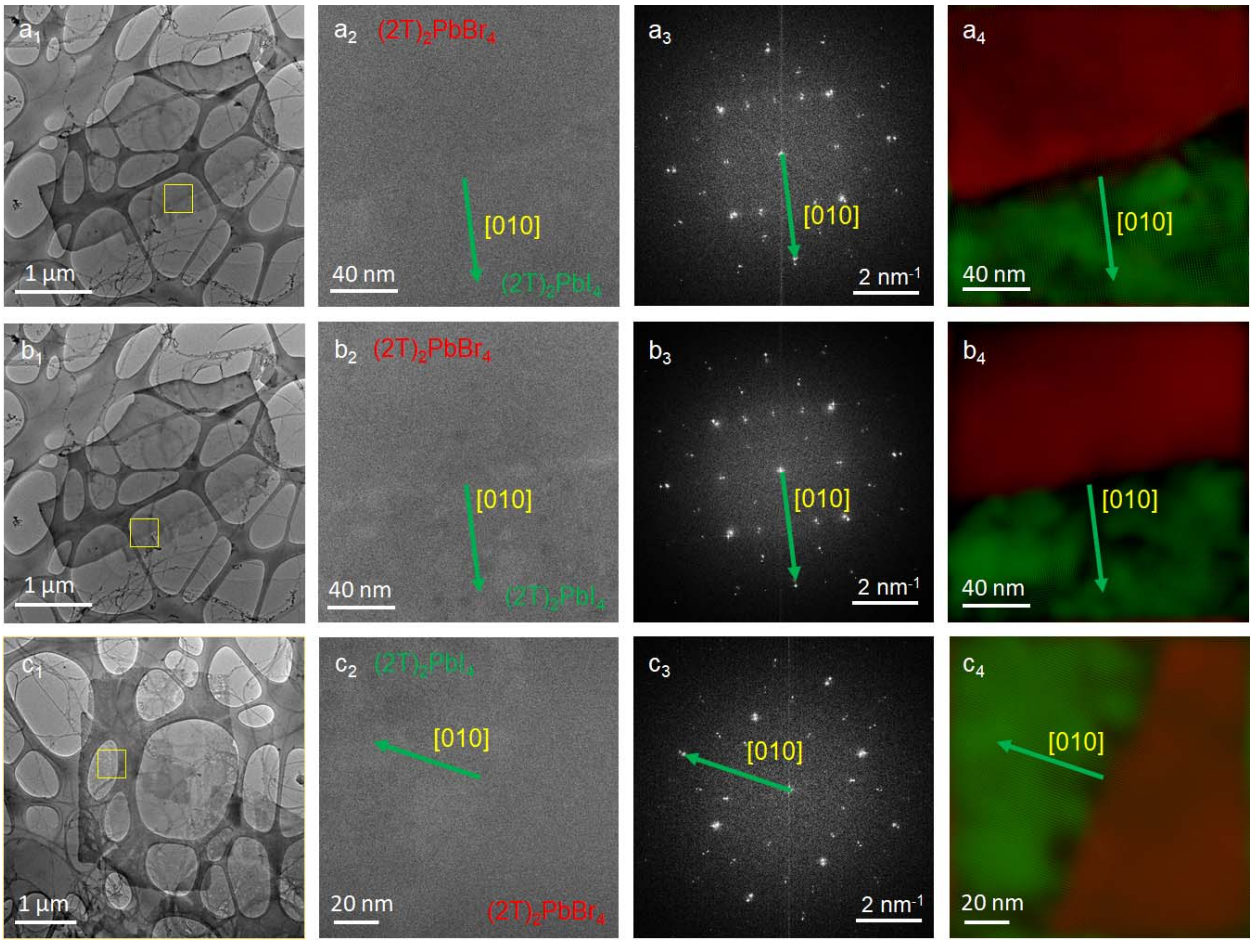

Supplementary Fig. 18 | Analysis of the epitaxial growth. a_1, b_1, c_1, Low-magnification TEM images of $2T)_2PbI_4$-$(2T)_2PbBr_4$ heterostructures. **a_2, b_2, c_2**, AC-HRTEM images. **a_3, b_3, c_3**, ~~F~~FT patterns. **a_4, b_4, c_4**, Inverse ~~F~~FT images highlighting $(2T)_2PbI_4$ and $(2T)_2PbBr_4$ lattices. These results show that the $(2T)_2PbI_4$ preferentially grew along two certain directions ([010] and [100]).

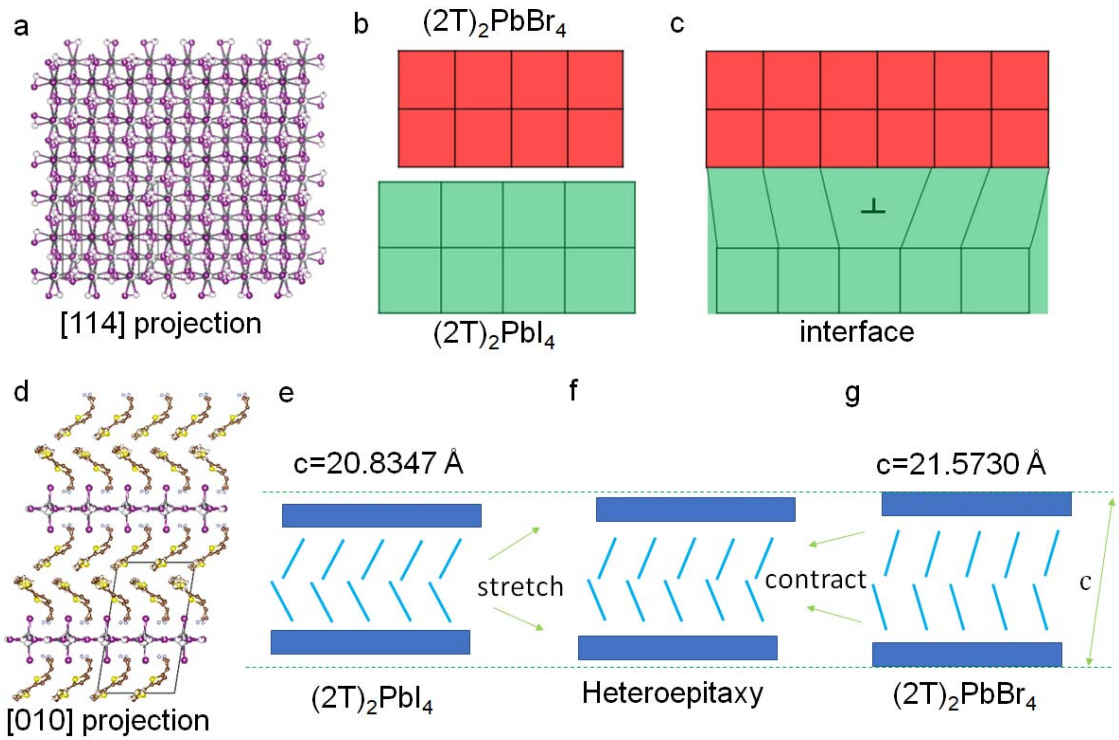

Supplementary Fig. 19 | The heteroepitaxy structure of $(2T)_2PbI_4$-$(2T)_2PbBr_4$ heterostructure. a, The structural model of $(2T)_2PbI_4$ in [114] projection. **b,** Schematic illustration of lattices of pure $(2T)_2PbI_4$ and pure $(2T)_2PbBr_4$. The lattice misfit in (001) plane is about 5%. **c,** The schematic diagram of edge dislocation in (001) plane. **d,** The structural model of $(2T)_2PbI_4$ in [010] projection. **e,** The schematic diagram of pure $(2T)_2PbI_4$ with shorter c axis. **f,** Our proposed structure of the interface. **g,** The schematic diagram of pure $(2T)_2PbI_4$ with longer c axis. The lattice misfit is about 3.4% in the [001] direction. The misfit along [001] direction is mainly from the organic ligands and the interfacial stress along this direction is believed to be easier to release because of the softness of the organic layers.

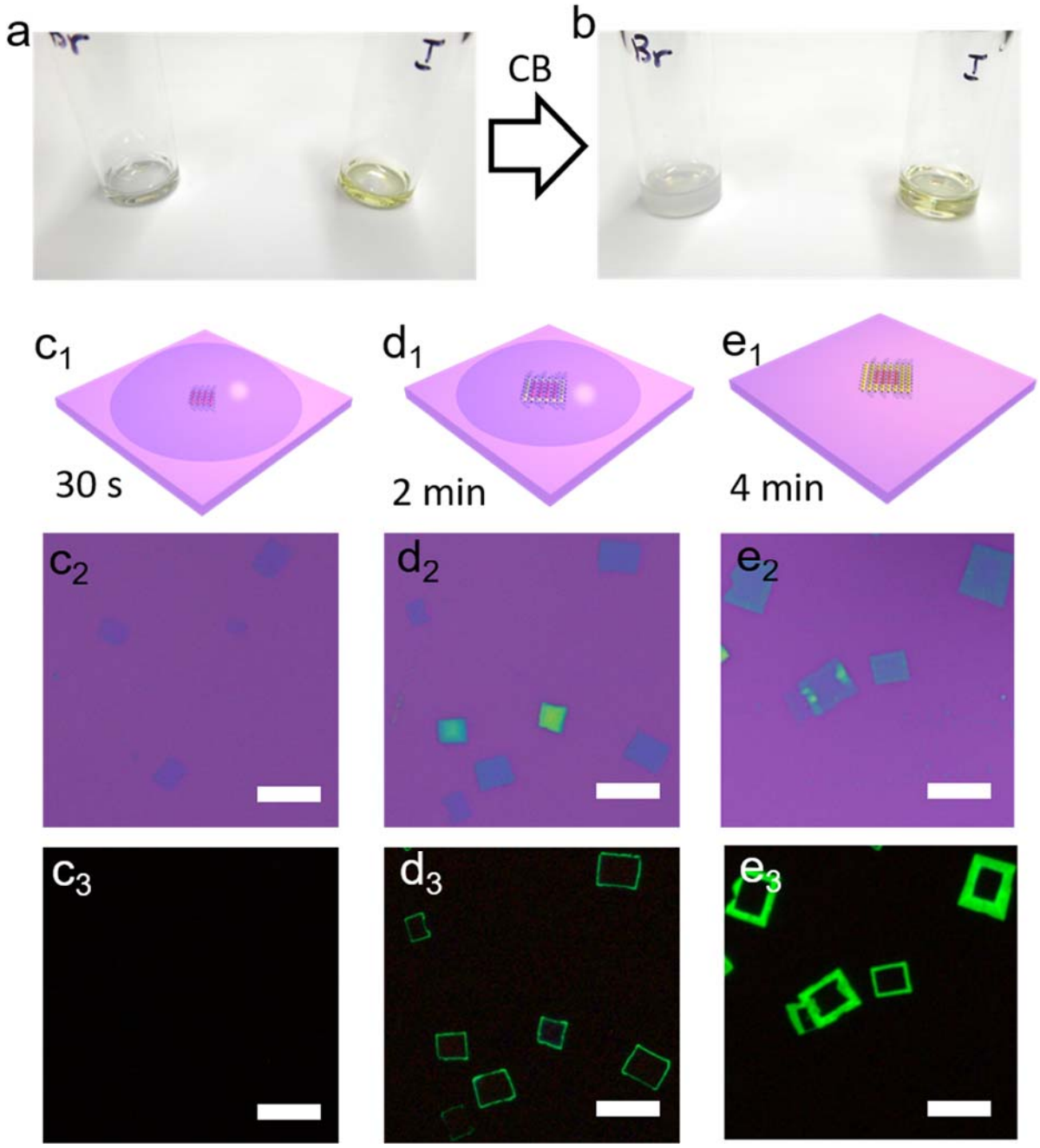

Supplementary Fig. 20 | One-pot synthesis of $(2T)_2PbI_4$-$(2T)_2PbBr_4$ lateral heterostructures. **a, b,** Photo images of $(2T)_2PbI_4$ and$(2T)_2PbBr_4$ stock solution before and after adding extra chlorobenzene (CB). **c-e**, Tracking of crystal nucleation process of $(2T)_2PbI_4$-$(2T)_2PbBr_4$ lateral heterostructures using one-pot synthesis strategy. **c**, Nucleated crystals after 30 seconds' growth; **d**, Nucleated crystals after 2 min's growth; **e**, Nucleated crystals after 4 min's growth. $\mathbf{c_1}$, $\mathbf{d_1}$ and $\mathbf{e_1}$, are schematics after different growth time; $\mathbf{c_2}$, $\mathbf{d_2}$, $\mathbf{e_2}$, and $\mathbf{c_3}$, $\mathbf{d_3}$, $\mathbf{e_3}$ are the corresponding bright-field and PL images, respectively. To characterize the intermediate products, the residue solvent left on the substrate was blown away by nitrogen. The scale bars are 10 μm.

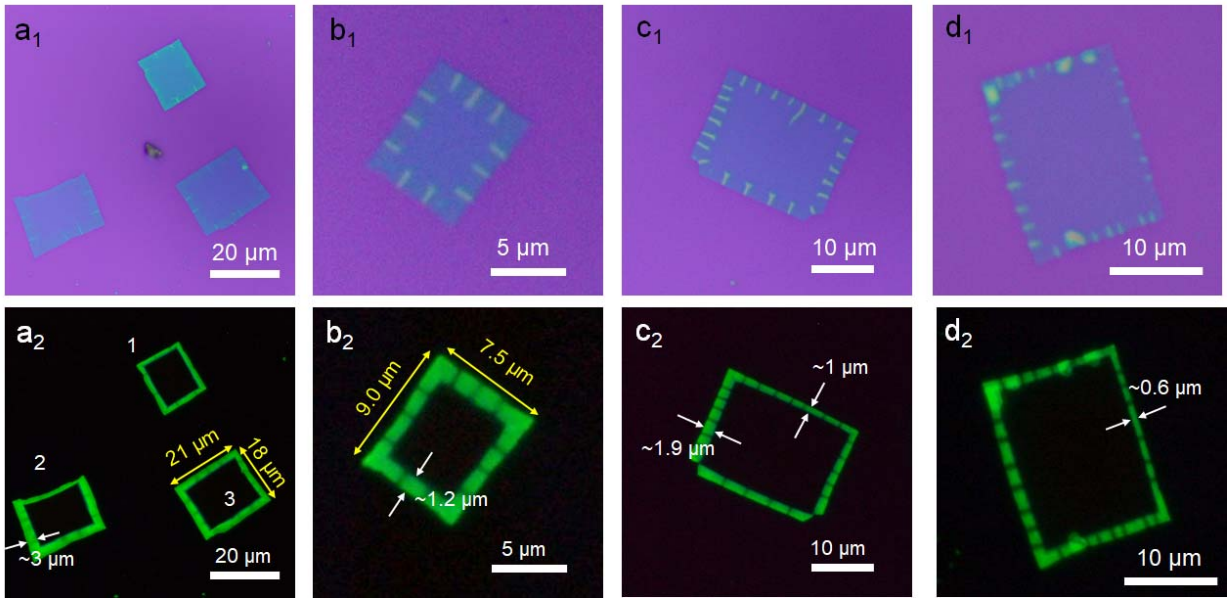

Supplementary Fig. 21 | Qualitative analysis of the ripples in one-pot $(2T)_2PbI_4$-$(2T)_2PbBr_4$ lateral heterostructures. Optical and PL images of 4 sets of one-pot $(2T)_2PbI_4$-$(2T)_2PbBr_4$ lateral heterostructures. Despite the big difference in width of $(2T)_2PbI_4$ domains, periodic ripples have been successfully formed, indicating the formation of ripples is among the primary strain relaxation mechanisms in all these heterostructures. The high tolerance of ripple formation to the lateral size and thickness in one-pot $(2T)_2PbI_4$-$(2T)_2PbBr_4$ heterostructures may arise from the soft lattice and high defect tolerance nature in 2D halide perovskites.

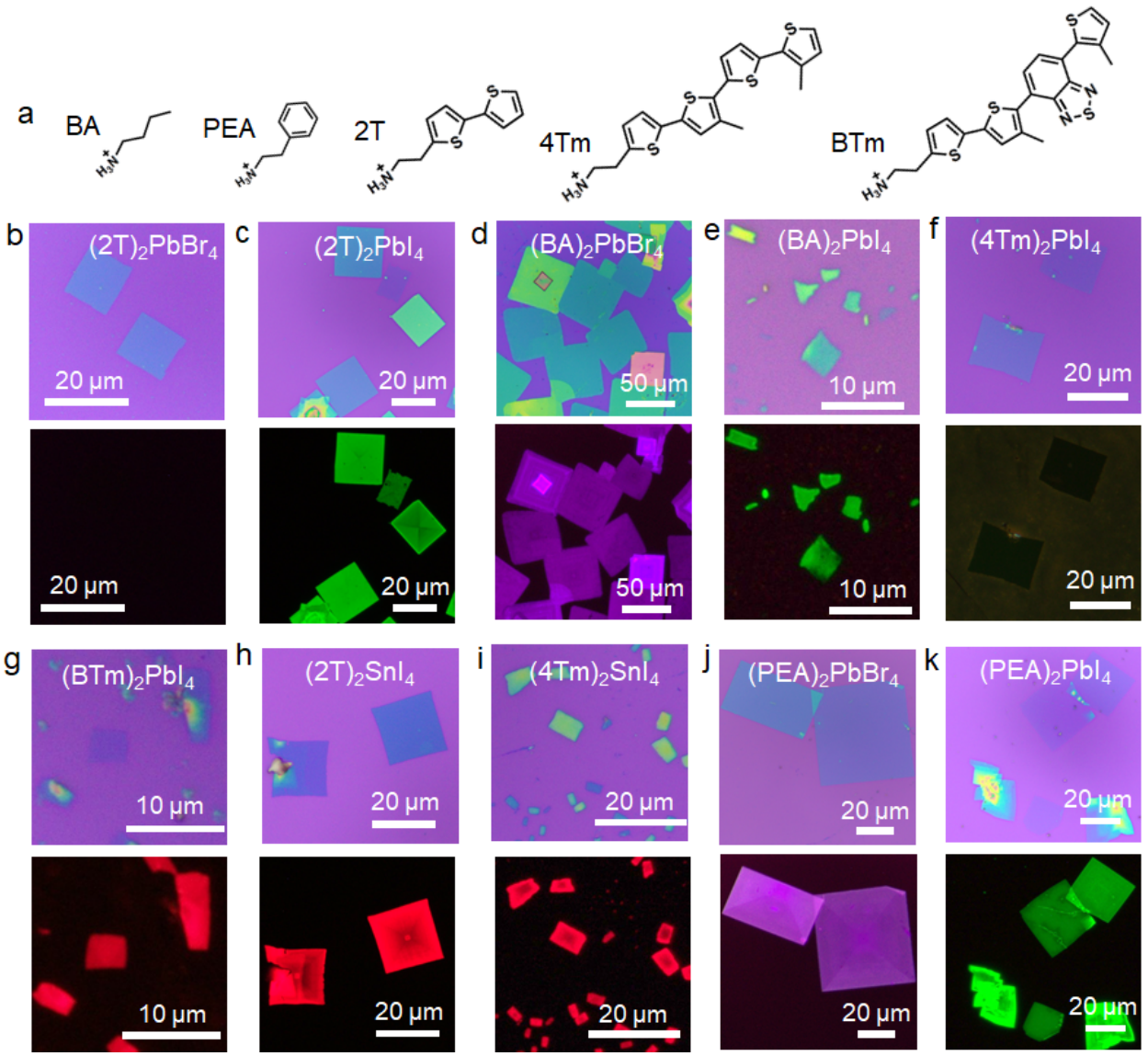

Supplementary Fig. 22 | Optical and PL images of 10 types of pure 2D halide perovskite sheets. **a,** Organic ligands involved in the 2D perovskites and heterostructures synthesis in our study, including BA^+, PEA^+, $2T^+$, $4Tm^+$ and BTm^+ ligands. **b,** Optical and PL images of $(2T)_2PbBr_4$ sheets. The PL emission is quenched due to type-II band alignment between the inorganic $[PbBr_4]^{2-}$and organic ligand $2T^+$ layers. **c,** Optical and PL images of $(2T)_2PbI_4$ sheets. **d,** Optical and PL images of $(BA)_2PbBr_4$ sheets. **e,** Optical and PL images of $(BA)_2PbI_4$ sheets. **f,** Optical and PL images of $(4Tm)_2PbI_4$ sheets. The PL emission is quenched due to type-II band alignment between the inorganic $[PbI_4]^{2-}$and organic ligand $4Tm^+$ layers. **g,** Optical and PL images of $(BTm)_2PbI_4$ sheets. The red emission comes from organic ligand BTm^+ layer as $[PbI_4]^{2-}$ and $4Tm^+$ layers form type-I band alignment and BTm^+ layer possesses lower bandgap. **h,** Optical and PL images of $(2T)_2SnI_4$ sheets. **i,** Optical and PL images of $(4Tm)_2SnI_4$ sheets. **j,** Optical and PL images of $(PEA)_2PbBr_4$ sheets. **k,** Optical and PL images of $(PEA)_2PbI_4$ sheets.

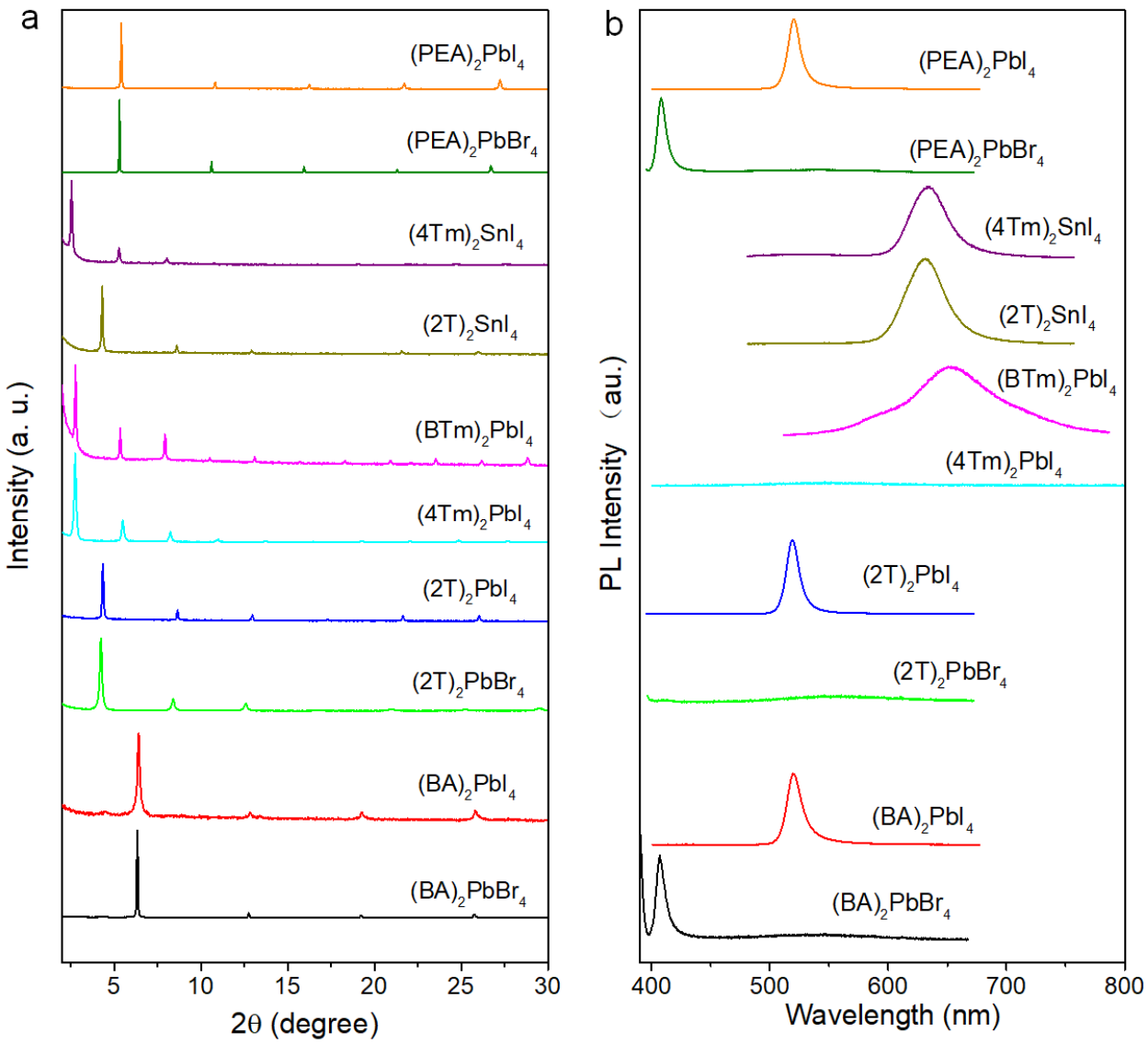

Supplementary Fig. 23 | XRD profiles (a) and PL spectra (b) of 10 types of pure 2D halide perovskite sheets. The periodic XRD peaks of these 2D halide perovskite sheets are indications of layered structures, and the interlayer spacings can be calculated from these peaks. All the sheets except $(2T)_2PbBr_4$ and $(4Tm)_2PbI_4$, have strong PL emission, which is consistent with corresponding PL images in Supplementary Fig. 22.

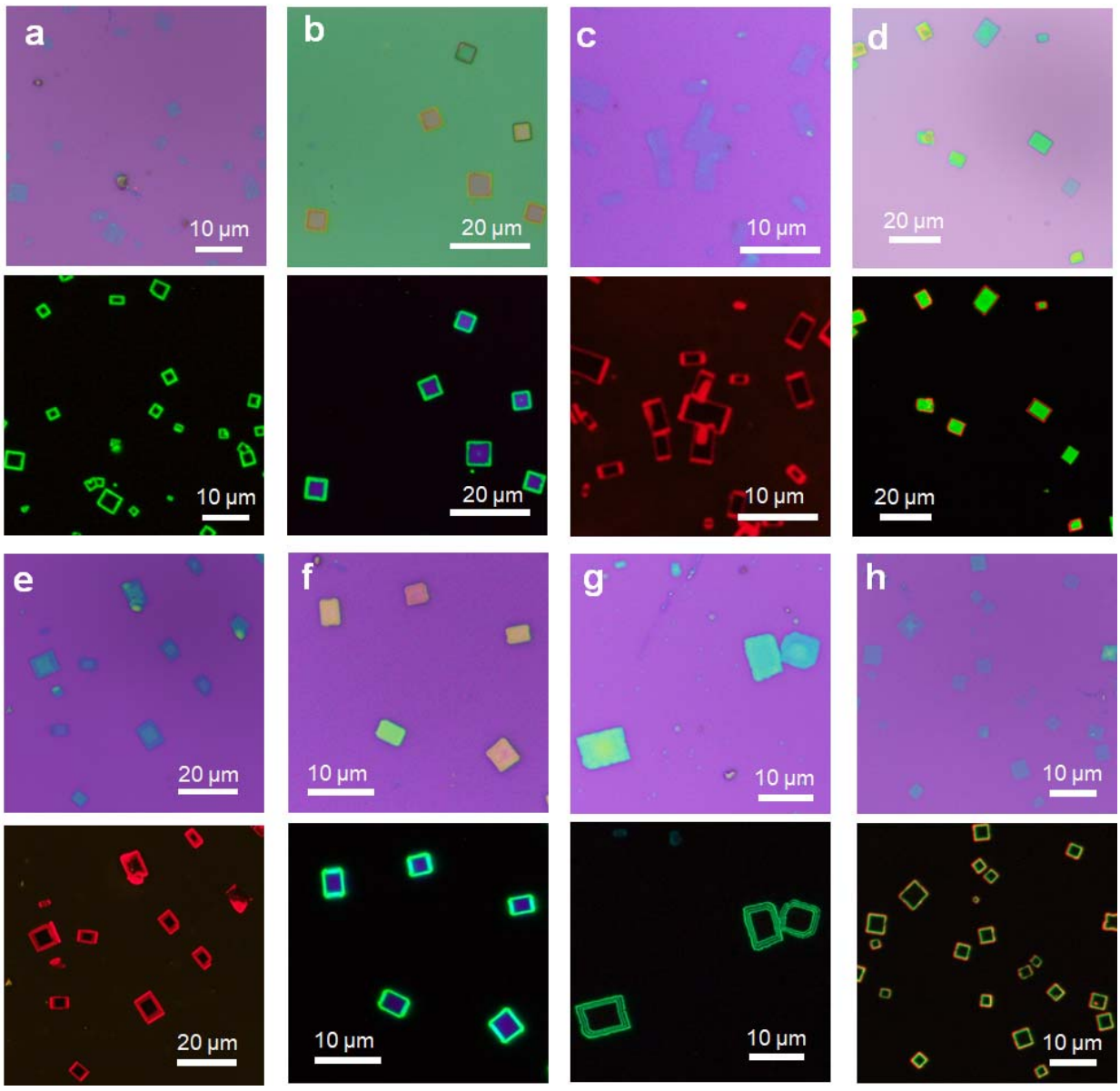

Supplementary Fig. 24 | Low- magnification optical and PL images of 8 types of lateral 2D halide perovskite heterostructures. a, $(2T)_2PbI_4$-$(2T)_2PbBr_4$. **b,** $(BA)_2PbI_4$-$(BA)_2PbBr_4$. **c,** $(BTm)_2PbI_4$-$(4Tm)_2PbI_4$. **d,** $(2T)_2SnI_4$-$(2T)_2PbI_4$. **e,** $(4Tm)_2SnI_4$-$(4Tm)_2PbI_4$. **f,** $(PEA)_2PbI_4$-$(PEA)_2PbBr_4$. **g,** $(2T)_2PbI_4$-$(2T)_2PbBr_4$-$(2T)_2PbI_4$-$(2T)_2PbBr_4$-$(2T)_2PbI_4$-$(2T)_2PbBr_4$. **h,** $(2T)_2SnI_4$-$(2T)_2PbI_4$-$(2T)_2PbBr_4$. These images indicate that the yields of various 2D lateral halide perovskite heterostructures synthesis are quite high.

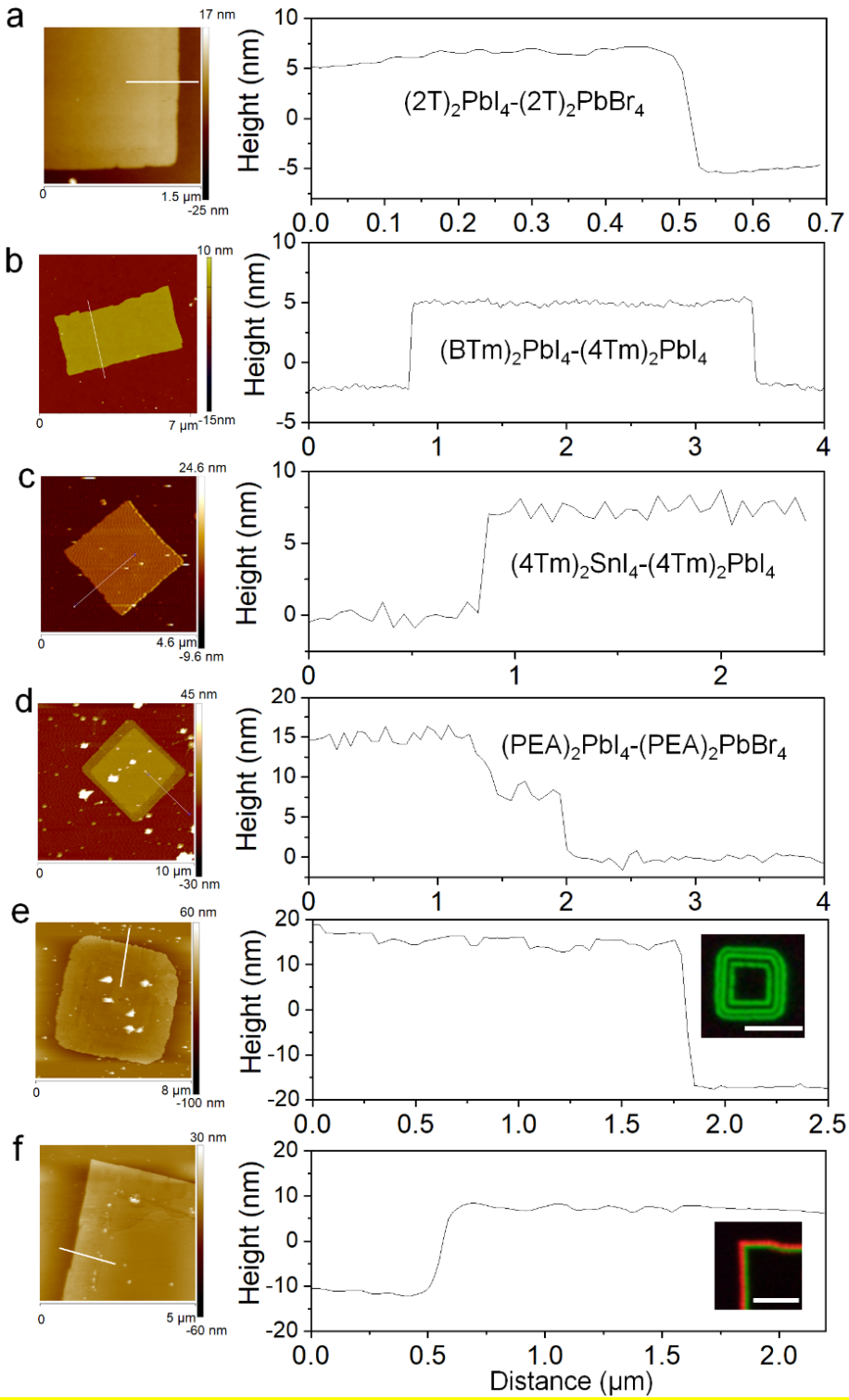

Supplementary Fig. 25 | AFM characterizations of 2D lateral halide perovskite heterostructures. AFM images and height profiles of: **a,** $(2T)_2PbI_4$-$(2T)_2PbBr_4$; **b,** $(BTm)_2PbI_4$-$(4Tm)_2PbI_4$; **c,** $(4Tm)_2SnI_4$-$(4Tm)_2PbI_4$; **d,** $(PEA)_2PbI_4$-$(PEA)_2PbBr_4$; **e**, $(2T)_2PbI_4$-$(2T)_2PbBr_4$ ×3; **f**, $(2T)_2SnI_4$-$(2T)_2PbI_4$-$(2T)_2PbBr_4$ heterostructures. Insets are the corresponding PL images. The scale bars are 5 μm. The height difference between $(PEA)_2PbI_4$ and $(PEA)_2PbBr_4$ is induced by the poor stability of thin $(PEA)_2PbI_4$ sheets in ambient environment.

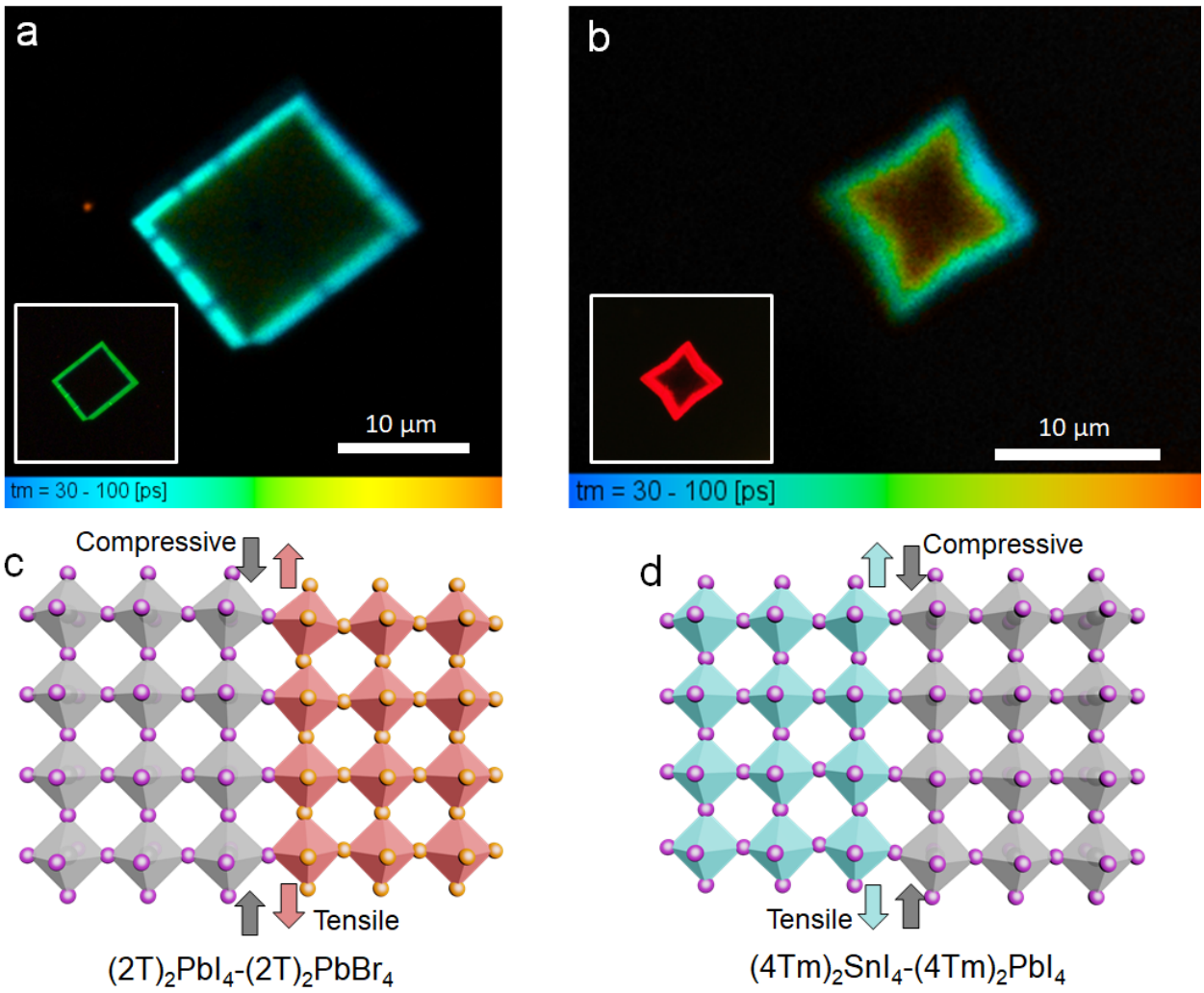

Supplementary Fig. 26 | FLIM characterization of $(2T)_2PbI_4$-$(2T)_2PbBr_4$ (a) and $(4Tm)_2SnI_4$-$(4Tm)_2PbI_4$ (b) heterostructures. The longer exciton lifetime at the interface of the heterostructures observed in fluorescence lifetime imaging measurements shed light on the possibility of tuning the optoelectronic properties *via* strain engineering at the interfaces. Insets are the corresponding PL images. The corresponding lattice parameters are summarized in Supplementary Table 1 and 4. **c, d,** Schematic illustrations of the tensile and compressive strains at the interface of $(2T)_2PbI_4$-$(2T)_2PbBr_4$ (**c**) and $(4Tm)_2SnI_4$-$(4Tm)_2PbI_4$ (**d**) heterostructures. For clarity, the organic ligands have been omitted.

Supplementary Tables

Supplementary Table 1| Single crystal X-ray diffraction data of $(2T)_2PbI_4$ and $(2T)_2PbBr_4$

	$(2T)_2PbI_4$	**$(2T)_2PbBr_4$**
Crystal data		
Chemical formula	$PbI_4 \cdot 2(C_{10}H_{12}NS_2)$	$Br_8Pb_2 \cdot 4(C_{10}H_{12}NS_2)$
M_r	1135.44	1894.96
Crystal system, space group	Triclinic, P1	Triclinic, $P\bar{1}$
Temperature (K)	150	150
a, *b*, *c* (Å)	12.0933(7), 12.2631(7), 20.8347(12)	11.3032 (13), 11.6338 (13), 21.602 (2)
α, β, γ (°)	98.415(2), 98.940(2), 90.003(2)	82.260 (4), 86.069 (5), 89.888 (5)
V (Å^3)	3018.6(3)	2808.0 (5)
Z	4	2
Radiation type	Cu *Kα*	Cu *Kα*
μ (mm^{-1})	45.67	21.23
Crystal size (mm)	0.12 × 0.10 × 0.02	0.21 × 0.15 × 0.01
Data collection		
Diffractometer	Bruker AXS D8 Quest CMOS diffractometer	Bruker AXS D8 Quest CMOS diffractometer
Absorption correction	Multi-scan SADABS 2016/2: Krause, L., Herbst-Irmer, R., Sheldrick G.M. & Stalke D., J. Appl. Cryst. 48 (2015) 3-10	Multi-scan TWINABS 2012/1: Krause, L., Herbst-Irmer, R., Sheldrick G.M. & Stalke D. (2015). J. Appl. Cryst. 48 3-10.
T_{min}, T_{max}	0.065, 0.233	0.039, 0.174
No. of measured, independent and observed [$I > 2\sigma(I)$] reflections	29414, 16616, 14142	81449, 11565, 9366
R_{int}	0.095	0.218
$(\sin \theta/\lambda)_{max}$ (Å^{-1})	0.639	0.631
Refinement		
$R[F^2 > 2\sigma(F^2)]$, $wR(F^2)$, *S*	0.080, 0.226, 1.03	0.123, 0.332, 1.04
No. of reflections	16616	11565
No. of parameters	1605	571
No. of restraints	4055	
H-atom treatment	H-atom parameters constrained	H-atom parameters constrained
$\Delta\rho_{max}$, $\Delta\rho_{min}$ (e Å^{-3})	4.73, -3.86	4.69, -2.60
Absolute structure	Twinning involves inversion, so Flack parameter cannot be determined	
Absolute structure parameter	0.25(2)	

Computer programs: Apex3 v2017.3-0 (Bruker, 2016), SAINT V8.37A (Bruker, 2016), SHELXS97 (Sheldrick, 2008), SHELXL2018/3 (Sheldrick, 2015, 2018), SHELXLE Rev924 (Hübschle et al., 2011).

Supplementary Table 2| Crystal lattice constant comparison of $(BA)_2PbBr_4$, $(BA)_2PbI_4$, $(2T)_2PbBr_4$ and $(2T)_2PbI_4$

2D Perovskite	*c* (Å)	Average Pb-Pb distance in x-y plane (Å)	Temperature (K)
$(BA)_2PbBr_4$	27.6	5.85	298
$(BA)_2PbI_4$	26.2	6.60	223
$(2T)_2PbBr_4$	21.6	5.85	150
$(2T)_2PbI_4$	20.8	6.06	150

Supplementary Table 3| Lattice misfit in (001) plane between $(2T)_2PbBr_4$ and $(2T)_2PbI_4$ obtained *via* different methods

Methods	Description	Misfit (%)
SAED patterns: between 2 pure phases	Calculated from SAED patterns of pure $(2T)_2PbI_4$ and $(2T)_2PbBr_4$ (Supplementary Fig. 13b, d), along [010] direction	5.9
	Calculated from SAED patterns of pure $(2T)_2PbI_4$ and $(2T)_2PbBr_4$ (Supplementary Fig. 13b, d), along [100] direction	5.7
SAED patterns: Between 2 segments in heterostructure	Calculated from SAED pattern of the heterostructure (Supplementary Fig. 13f), along [010] direction	4.8
	Calculated from SAED pattern of the heterostructure (Supplementary Fig. 13f), along [100] direction	5.0
~~F~~FT patterns: Between 2 segments in heterostructure	Calculated from ~~F~~FT pattern of AC-HRTEM (Fig. 2b), along [010] direction	5.4
	Calculated from ~~F~~FT pattern of AC-HRTEM (Fig. 2b), along [100] direction	5.9
MD simulation: Between 2 pure phases	Calculated from molecular dynamic simulation	5.7
MD simulation: Between 2 segments in heterostructure	Calculated from molecular dynamic simulation	3.6

Supplementary Table 4| Single crystal X-ray diffraction data of $(4Tm)_2PbI_4$ and $(4Tm)_2SnI_4$

	$(4Tm)_2PbI_4$	$(4Tm)_2SnI_4$
Crystal data		
Chemical formula	$2(C_{20}H_{20}NS_4)\cdot I_3Pb\cdot I$	$I_{16}Sn_4\cdot 8(C_{20}H_{20}NS_4)$
M_r	1520.01	1431.51
Crystal system, space group	Monoclinic, *C*2/*c*	Triclinic, *P*1
Temperature (K)	150	150
a, *b*, *c* (Å)	64.191 (6), 6.0936 (5), 12.2111 (9)	12.0929 (5), 12.1407 (6), 32.4960 (15)
α, β, γ (°)	97.773 (4)	84.6775 (16), 82.8330 (15), 89.9763 (15)
V (Å^3)	4732.5 (7)	4713.0 (4)
Z	4	4
Radiation type	Cu *K*α	Cu *K*α
μ (mm^{-1})	30.96	28.44
Crystal size (mm)	0.13 × 0.09 × 0.02	0.45×0.35×0.04
Data collection		
Diffractometer	Bruker AXS D8 Quest CMOS diffractometer	Bruker AXS D8 Quest CMOS diffractometer
Absorption correction	Multi-scan SADABS 2016/2: Krause, L., Herbst-Irmer, R., Sheldrick G.M. & Stalke D. (2015). J. Appl. Cryst. 48 3-10.	Multi-scan SADABS 2016/2: Krause, L., Herbst-Irmer, R., Sheldrick G.M. & Stalke D. (2015). J. Appl. Cryst. 48 3-10.
T_{min}, T_{max}	0.079, 0.576	0.036, 0.169
No. of measured, independent and observed [$I > 2\sigma(I)$] reflections	19108, 19108, 10800	39643, 24865, 19004
R_{int}	0.089	0.092
$(\sin\theta/\lambda)_{max}$ (Å^{-1})	0.641	0.61
Refinement		
$R[F^2 > 2\sigma(F^2)]$, $wR(F^2)$, S	0.118, 0.377, 1.10	0.138, 0.413, 1.10
No. of reflections	19108	24865
No. of parameters	294	1974
No. of restraints	81	3976
H-atom treatment	H-atom parameters constrained	H-atom parameters constrained
$\Delta\rho_{max}$, $\Delta\rho_{min}$ (e Å^{-3})	3.54, −2.30	5.43, -3.95
Absolute structure		Twinning involves inversion, so Flack parameter cannot be determined

Computer programs: Apex3 v2016.9-0 (Bruker, 2016), SAINT V8.37A (Bruker, 2016), SHELXS97 (Sheldrick, 2008), SHELXL2018/1 (Sheldrick, 2015, 2018), SHELXLE Rev882 (Hübschle et al., 2011), SHELXL2018/3 (Sheldrick, 2015, 2018), SHELXLE Rev937 (Hübschle et al., 2011).

References

1 Yu, Y. *et al.* Atomic resolution imaging of halide perovskites. *Nano Lett.*, **16**, 7530-7535, (2016).

2 Zhang, D. *et al*. Ultrathin colloidal cesium lead halide perovskite nanowires. *J. Am. Chem. Soc*. **138**, 13155-13158, (2016).

3 Yu, Y. *et al*. Ruddlesden–popper phase in two-dimensional inorganic halide perovskites: a plausible model and the supporting observations. *Nano Lett.* **17**, 5489-5494 (2017).

4 Dou, L. *et al.* Atomically thin two-dimensional organic-inorganic hybrid perovskites. *Science* **349**, 1518-1521 (2015).

5 Hÿtch, M., Snoeck, E. & Kilaas, R. Quantitative measurement of displacement and strain fields from HREM micrographs. *Ultramicroscopy* **74**, 131-146 (1998).

6 Hÿtch, M. J., Putaux, J.-L. & Pénisson, J.-M. Measurement of the displacement field of dislocations to 0.03 Å by electron microscopy. *Nature* **423**, 270 (2003).

7 Xie, S. *et al.* Coherent, atomically thin transition-metal dichalcogenide superlattices with engineered strain. *Science* **359**, 1131-1136 (2018).

8 Liu, Y., Huang, Y. & Duan, X. Van der Waals integration before and beyond two-dimensional materials. *Nature* **567**, 323 (2019).

9 Matthews, J. & Blakeslee, A. Defects in epitaxial multilayers: I. Misfit dislocations. *Journal of Crystal growth* **27**, 118-125 (1974).